

# UC San Diego

## UC San Diego Electronic Theses and Dissertations

### Title

Non-degenerated two photon excitation for fluorescence microscopy in the scattering media

### Permalink

<https://escholarship.org/uc/item/6108d1p4>

### Author

Yang, Mu-Han

### Publication Date

2018

Peer reviewed|Thesis/dissertation

UNIVERSITY OF CALIFORNIA SAN DIEGO

Non-degenerated two photon excitation for fluorescence microscopy in the scattering  
media

A dissertation submitted in partial satisfaction of the  
requirements for the degree Doctor of Philosophy

in

Electrical Engineering (Photonics)

by

Mu-Han Yang

Committee in charge:

Professor Yeshaiah Fainman, Chair  
Professor Anna Devor, Co-Chair  
Professor Boubacar Kante  
Professor David Kleinfeld  
Professor Zhaowei Liu

2018

Copyright

Mu-Han Yang, 2018

All rights reserved.

The Dissertation of Mu-Han Yang is approved, and it is acceptable in quality and form for publication on microfilm and electronically:

---

---

---

---

---

Chair

University of California San Diego

2018

## TABLE OF CONTENTS

Signature Page .....	iii
Table of Contents .....	iv
List of Figures .....	vi
List of Tables .....	ix
Acknowledgements .....	x
Vita .....	xiii
Abstract of the Dissertation .....	xvi
Chapter 1 Introduction .....	1
Chapter 2 Non-degenerated two photon excitation .....	6
2.1 Background.....	6
2.2 Materials and Methods .....	8
2.2.1 Fluorophores for brain image .....	8
2.2.2 Non-degenerated two photon excitation Setup.....	9
2.2.3 Fluorescence generation with beam overlap.....	13
2.2.4 Non-degenerated two photon excitation cross section .....	16
2.3 Results.....	22
2.4 Discussion.....	26
2.5 Supplemental Materials .....	28
Acknowledgements .....	35
Chapter 3 Increased penetration depth with non-degenerated two photon excitation .....	36
3.1 Background.....	36
3.2 Increased penetration depth with non-degenerated two photon excitation .....	39
3.2.1 Sample preparation and characterization Setup .....	39
3.2.2 Demonstration of the increased penetration depth with ND-2PE .....	41
3.2.3 Experimental validation of penetration depth increase via ND-2PE....	44
3.4 Discussion.....	45
Acknowledgments .....	47
Chapter 4 Reduction of out-of-focus excitation.....	48

4.1	Background.....	48
4.2	Materials and Methods .....	53
4.2.1	Sample preparation and characterization setup .....	53
4.2.2	Examination of out-of-focus excitation .....	55
4.2.3	Characterization of ND-2PE volume with side-by-side beams .....	56
4.2.4	ND-2PE cross section with side-by-side beams .....	58
4.3	Results.....	60
4.4	Discussion.....	65
	Acknowledgements .....	67
	Chapter 5 Conclusion and Future Works.....	68
	Appendix A Intermediate State Resonance Enhancement by Essential State Model.....	70
A.1	Background.....	70
A.2	Methods .....	71
A.3	Acknowledgement .....	72
	Bibliography .....	73

## LIST OF FIGURES

<b>Figure 1.1</b> Schematic energy diagram demonstrating degenerate and non-degenerate multi-photon absorption of a molecule: (a) D-2PE; (b) D-3PE; and (c) ND-2PE.....	5
<b>Figure 2.1:</b> Widely used fluorophores in brain images which range from 700 nm to 1300 nm.....	9
<b>Figure 2.2:</b> Spectroscopy setup of ND-2PE. PBS, polarization beam splitter; HWP, half wave plate; DM, dichroic mirror; BE, beam expander; PD, photodetector; PT, power tape; M, mirror. ....	11
<b>Figure 2.3:</b> ND-2PE microscope. PBS, polarization beam splitter; HWP, half wave plate; DM, dichroic mirror; BE, beam expander; PD, photodetector; PT, power tape; M, mirror. ....	12
<b>Figure 2.4:</b> Layout of the homemade microscope. M, mirror; DM, dichroic mirror; OBJ, 20X microscope objective; BPF, band pass filter; PMT, photomultiplier; Amp, signal amplifier .....	13
<b>Figure 2.5:</b> Experimental demonstration of ND-2PE. (a) dependence of the fluorescence signal on temporal alignment; (b) fluorescence intensity dependence on NIR power; (c) fluorescence intensity dependence on SWIR power. ....	15
<b>Figure 2.6:</b> Spectroscopy of ND-2PE for fluorophores (eGFP, mCerulean, eYFP and mCitrine, fluorescein and coumarin-343) .....	24
<b>Figure 2.7:</b> Images of eGFP tagged mice brain under (a) D-2PE (b) ND-2PE.....	25
<b>Figure 2.8:</b> The histogram of the fluorescence signal under D-2PE and ND-2PE at the depth of 200 $\mu\text{m}$ . ....	26
<b>Figure 2.9:</b> The tuning range of Chameleon-OPO system.....	28
<b>Figure 2.10:</b> Experimental setup for resolving the intensity distribution of NIR beam and IR beam .....	29
<b>Figure 2.11:</b> Intensity distribution of NIR beam (green curve) and IR beam (red curve) at different axial position. ....	30
<b>Figure 2.12:</b> Fluorescence under D-2PE (red curve) and ND-2PE (blue curve) at different axial position. ....	31
<b>Figure 2.13:</b> The D-2PE spectrum for fluorophores reported in the literatures.....	32

<b>Figure 2.14:</b> Mount system for Mice heads.....	34
<b>Figure 3.1:</b> The attenuation length at different wavelength in brain tissues. ....	38
<b>Figure 3.2:</b> Experimental setup for demonstration of penetration depth of D-2PE and ND-2PE. ....	40
<b>Figure 3.3:</b> Relative fluorescence intensity as a function of sample depth within varying concentrations of intralipid: (a) 0.5 %, (b) 0.75%, (c) 1%, (d) 1.5 % and (e) 2%. (f) Attenuation length as a function of intralipid concentrations.....	42
<b>Figure 3.4:</b> Simulation of the fluorescence intensity under D-2PE (blue) and ND-2PE (green) as a function of depth in the scattering medium.....	44
<b>Figure 3.5:</b> Experimental demonstration that ND-2PE can excite fluorescence at greater depth.....	45
<b>Figure 3.6:</b> The transmission of brain tissue with different thickness. ....	47
<b>Figure 4.1:</b> The simulation for fluorescence generation at different depths. ....	50
<b>Figure 4.2:</b> Fluorescence signal in beads sample with D-2PE.....	50
<b>Figure 4.3:</b> Bead sample. (a) top view of the sample (b) side view of the sample.. ....	54
<b>Figure 4.4:</b> Experimental setup for investigating the fluorescence under D-2PE and ND-2PE with side-by-side beams .....	56
<b>Figure 4.5:</b> Experimental results of background to signal ration under D-2PE and ND-2PE with side-by-side beams .....	56
<b>Figure 4.6:</b> The intensity distribution of NIR beam and IR beam. The beam with larger size is the IR beam and the beam with smaller size is the NIR beam.....	57
<b>Figure 4.7:</b> Intensity distribution of side-by-side beams before objective lens (a) lateral resolution of side-by-side beams (b) axial resolution of side-by-side beams	58
<b>Figure 4.8:</b> Fluorescence signal under ND-2PE at different time delay with (a) collinear beams and (b) side-by-side beams .....	59
<b>Figure 4.9:</b> Images under D-2PE and ND-2PE with collinear beams at different depth (a) D-2PE (780 nm) (b) ND-2PE (780 nm and 1090 nm) (c) D-2PE (909 nm)..	61
<b>Figure 4.10:</b> Images under D-2PE and ND-2PE with side-by-side beams at different depth (a) D-2PE (780 nm) (b) ND-2PE (780 nm and 1090 nm) (c) D-2PE (909 nm).....	63

**Figure 4.11:** Line scan across one fluorescent bead under D-2PE and ND-2PE with side-by-side beams at the depth of 650  $\mu\text{m}$ (a) ND-2PE (780 nm and 1090) (b) D-2PE (909 nm) ..... 63

## LIST OF TABLES

<b>Table 2.1:</b> Summary of the center position of the NIR beam and IR beam at different axial position .....	31
<b>Table 2.2:</b> Simulation of the IRSE for some useful fluorophores.....	72

## ACKNOWLEDGEMENTS

This work would not be accomplished without all the help from my colleagues, mentors, and my two advisors, professor Fainman and professor Devor. My thesis is a cross-disciplinary project and it involves not only different expertise but also communication with people from different fields.

First, I would like to thank my advisors, professor Fainman and professor Devor. In addition to funding and resource support, they always were willing to accept any new idea and helped me to make a clear plan especially when there were many approaches for our project. While I joined this lab, I was not good at presenting my research but they were very patient with my explanation. Moreover, they both encouraged me to sharp my presentation skill in many conferences or symposiums. Those were priceless experiences in my PhD life. I also got some chances to review journal papers because of their recommendation and that lead me to look deep into a completed work. I really appreciated that they offer me so many invaluable resources to improve myself.

I would like to thank Dr. Maxim for helping me with starting the whole project. At the beginning, he gave me some good instructions by sending me many useful papers and explaining the preliminary setup. He spent much time on helping me to get familiar with the whole idea of this project. When I had any problem, he always responded immediately and that helped me to get involved in the project in a very short time. After Dr. Maxim left, Dr. Ferri joined our group to help me to continue the project. He was very knowledgeable in optics field and we worked together to build a prototype non-degenerated two photon microscope which was very important for our future experiments. He is not only a good

colleague but also a true friend to me. Dr. Sadegh joined our project in my last PhD year which was the busiest year to me. I really want to thank her for encouraging me and listening to me when I was overwhelmed with the workload. She is a very logical and well-organized person so whenever I was confused with the priority of multiple tasks I could always come up with a clear plan after discussing with her. Dr. Thunemann is one of the most humorous and intelligent scientists I have ever meet and he was actually solving most of my problems with biological samples. He always was willing to spending his time on my project no matter how busy he was. Dr. Kilic was the first one in professor Devor's lab to prepare fluorophore for me. She was always kind when I asked nonprofessional questions about the sample preparation. I would also like to thank for my friends and labmates in professor Fainman's lab. Dr. Lin, Cheng-yi Fang, and Brandon Hong . They liked to share the experimental experiences and chat with me after we released from our works. The last but not the least, I would like to thank my parents for supporting me always.

Chapter 2 covers the work of non-degenerate 2-photon microscopy which demonstrate the enhancement of excitation cross section. Chapter 2, in part is currently being prepared for submission for publication of the material. Chris Ferri; Mu-Han Yang; Sanaz Sadegh; Martin Thunemann; Payam Saisan; Anna Devor; Yeshaiahu Fainman. The dissertation author was the investigator and author of this material.

Chapter 3 covers the materials from "Non-degenerate 2-photon excitation in scattering medium for fluorescence microscopy" by Mu-Han Yang, Maxim Abashin, Payam Saisan, Peifan Tian, Chris Ferri, Anna Devor, and Yeshaiahu Fainman, which was published in Optics Express. The dissertation author was the investigator and author of this

paper.

Chapter 4 covers the work of reduction of out-of-focus excitation which is achieved by displacing two beams. Chapter 4, in part is currently being prepared for submission for publication of the material. Mu-Han Yang; Sanaz Sadegh; Payam Saisan; Martin Thunemann; Chris Ferri; Anna Devor; Yeshaiahu Fainman. The dissertation author was the primary investigator and author of this material.

## VITA

- 2007            B. S. in Electrical Engineering, National Tsing Hua University, Taiwan.
- 2009            M. S. in Electrical Engineering, National Taiwan University, Taiwan
- 2018            Ph. D. in Electrical Engineering (Photonics), University of California  
San Diego, La Jolla.

## PUBLICATIONS

### Journal Article:

- Smolyaninov, Alexei, Mu-Han Yang, Lin Pang, and Yeshaiahu Fainman.  
"Plasmonic enhanced two-photon absorption in silicon photodetectors for optical correlators in the near-infrared." *Optics letters* 41, no. 19 (2016): 4445-4448.
- Yang, Mu-Han, Maxim Abashin, Payam A. Saisan, Peifang Tian, Christopher GL Ferri, Anna Devor, and Yeshaiahu Fainman. "Non-degenerate 2-photon excitation in scattering medium for fluorescence microscopy." *Optics express* 24, no. 26 (2016): 30173-30187.
- Puckett, Matthew W., Rajat Sharma, Hung-Hsi Lin, Mu-han Yang, Felipe Vallini, and Yeshaiahu Fainman. "Observation of second-harmonic generation in silicon nitride waveguides through bulk nonlinearities." *Optics express* 24, no. 15 (2016): 16923-16933.

- Lin, Hung-Hsi, Mu-Han Yang, Rajat Sharma, Matthew W. Puckett, Sergio Montoya, Christian D. Wurm, Felipe Vallini, Eric E. Fullerton, and Yeshaiahu Fainman. "Synthesis of second-order nonlinearities in dielectric-semiconductor-dielectric metamaterials." *Applied Physics Letters* 110, no. 11 (2017): 113103.
- Lin, Hung-Hsi, Felipe Vallini, Mu-Han Yang, Rajat Sharma, Matthew W. Puckett, Sergio Montoya, Christian D. Wurm, Eric E. Fullerton, and Yeshaiahu Fainman. "Electronic metamaterials with tunable second-order optical nonlinearities." *Scientific Reports* 7, no. 1 (2017): 9983.

Conference paper:

- Yang, Mu-Han, Christopher GL Ferri, Payam A. Saisan, Maxim Abashin, Peifang Tian, Yeshaiahu Fainman, and Anna Devor. "Multicolor two-photon excitation for increasing fluorescence excitation depth." In *Optics and the Brain*, pp. BrM4B-6. Optical Society of America, 2017.
- Yang, Mu-Han, Maxim Abashin, Payam Saisan, Anna Devor, and Yeshaiahu Fainman. "Non-degenerate multiphoton microscopy for deep brain imaging." In *Optics and the Brain*, pp. BrW3B-6. Optical Society of America, 2015.

- Lin, Hung-Hsi, Rajat Sharma, Mu-Han Yang, Matthew W. Puckett, Christian D. Wurm, Felipe Vallini, and Yeshaiahu Fainman. "Enhanced Effective Second-order Nonlinearities in Si-rich SiNx Thin Films." In *CLEO: Science and Innovations*, pp. SM1M-6. Optical Society of America, 2017.

## ABSTRACT OF THE DISSERTATION

Non-degenerated two photon excitation for fluorescence microscopy in the scattering media

by

Mu-Han Yang

Doctor of Philosophy in Electrical Engineering (Photonics)

University of California, San Diego 2018

Professor Yeshaiah Fainman, Chair

Two-photon microscopy has had an enormous influence on animal studies of in vivo brain activity providing a tool for high-resolution imaging in live cortical tissue. Yet, the majority of 2-photon imaging studies, as of today, have focused on the top  $\sim 500$   $\mu\text{m}$  of the cerebral cortex due to limited penetration of light into biological tissues. Cerebral neurons, however, are wired in circuits spanning the entire cortical depth ( $\sim 1$  mm in mice), and sampling of activity throughout this depth would be required for reconstruction of circuit dynamics. Therefore, increasing the in vivo penetration depth of microscopic imaging is at the heart of brain initiative society. In this thesis, we demonstrate that the degree of freedom introduced by non-degenerate 2-photon excitation (ND-2PE), using two

independently controlled pulsed laser sources of different photon energies, may provide a number of advantages over the conventional methods promising deeper penetration with higher efficiency of excitation and better signal-to-background ratio in a scattering medium.

The presence of two laser beams allows:

- 1) Tuning the combination of wavelengths to optimize excitation cross-section for each fluorophore;
- 2) Independent control of power (and polarization) such that an increase in the IR power can be used to compensate for the loss of NIR power due to scattering and absorption;
- 3) Spatial displacement of the two beams to limit the overlap to the focal volume, minimizing background excitation;

All the advantages are validated with our experiments in this thesis. We started with investigating the cross section of widely used fluorophores under ND-2PE. The experimental results showed the enhancement to the cross-section of ND-2PE in comparison with that of D-2PE. An experiment for neuron images in a mouse brain also supported the fact that signal enhancement was increased under ND-2PE. Next, we demonstrated that ND-2PE can increase maximum excitation depth in a scattering phantom by compensating the loss of NIR beam with IR beam. Finally, we demonstrated that the out-of-focus excitation in scattering phantom can be reduced by strategically displacing two beams. The scheme of side-by-side beams was also applied to in vivo brain images.

# CHAPTER 1

## INTRODUCTION

Two-photon microscopy has become a prominent technique in the application of brain image because of the features of small excitation volume, low attenuation, and background rejection as compared to conventional single-photon microscopy. By using two-photon microscopy, the depth of brain images up to few hundred microns could be achieved [1]. However, deeper images require high power and good image contrast which is limited by the scattering properties in brain tissues. Especially, white matter in brain tissues creates a barrier between cortex and hippocampus and this makes excitation of fluorophores in hippocampus very difficult [2]. As a result, less power can be delivery into the target plane and most of the input power contributes to huge amount of background signal. Therefore, many approaches have been proposed to overcome these issues.

Conventional 2-photon microscopy relies on absorption of two identical energy photons (i.e., degenerate 2PE (D-2PE), Fig. 1.1(a)). The light source, usually a pulsed femtosecond Ti:Sapphire laser, is tuned within the ~740-1000 nm near infrared (NIR) window. For example, 740 nm is used for imaging of nicotinamide adenine dinucleotide (NADH) [3,4] and 800-1000 nm for imaging of intravascular dextran-conjugated fluorescein isothiocyanate (FITC) [5]. Using even longer excitation wavelengths pushes the depth limit further due to an increase in the photon mean free path [6–8]. A recent study

using 1280 nm excitation documented imaging of mouse cortical vasculature in vivo down to ~1.6 mm [7] approximately reaching the fundamental depth limit in scattering tissue [9]. This wavelength, however, lies outside the D-2PE spectrum for most of the fluorophores currently used for brain imaging, thus limiting the approach to a handful of optical probes with far red emission (e.g., Alexa 680).

Another strategy to increasing imaging depth is the use of higher-order multiphoton excitation. Three-photon imaging relying on absorption of three equal energy photons (i.e., degenerate 3-photon excitation (D-3PE), Fig. 1.1(b)) at 1700 nm has been recently demonstrated to penetrate down to ~1.3 mm providing images of hippocampal neurons expressing red fluorescent protein [2]. Higher-order multiphoton excitation, however, suffers from very low absorption efficiency quantified by the 3-photon absorption cross-section [10,11], resulting in low emitted photon counts thus slowing down image acquisition. In addition, low fluorescence intensity is a significant drawback for real-time imaging of time resolved biological processes, e.g., neuronal activity. Furthermore, higher laser power needed to overcome the low D-3PE cross-section may harm tissue resulting from repeated dwelling on the same point as required for imaging of activity over time.

Finally, deeper subcortical imaging can be achieved using more invasive approaches such as microendoscopy [12], by removing the overlaying tissue [13], or with technologies that do not rely on optical focusing but at a price of decreased spatial resolution [14]. However, compromising the health of tissue or spatial resolution might not be an acceptable alternative for most cellular-level neuroscience applications.

To increase penetration depth, while avoiding low 3-photon excitation cross section, we explored ND-2PE – absorption of two photons of different energy [Fig. 1.1(c)]. Non-

degenerate excitation of optical species has a long history in the physical chemistry and microscopy communities [15–17]. Lakowicz et al. demonstrated that the fluorescence intensity of a sample can be enhanced at least 1000-fold through non-degenerate excitation. ND-2PE can have higher excitation cross because of intermediate state resonance enhancement (ISRE) [15]. Furthermore, they identified potential resolution gains as a result of the difference in spot sizes for each laser source. In addition, Lakowicz et al. proposed a method for rejecting background noise by detuning the repetition rate of each light source, resulting in beating of the fluorescence, which can be detected using a lock-in amplifier. Fu et al. subsequently demonstrated imaging using this repetition rate detuning scheme [18]. Cambaliza and Saloma [19], Ibáñez-López et al. [20], Blanca and Saloma [21], Xiao et al. [22], Caballero et al. [23], Wang et al. [24] and Deng et al. [25] have computed increased axial resolution of ND-2PE over D-2PE using various constructed illumination geometries. Kobat et al. [6] demonstrated an increase in axial resolution using ND-2PE via side-by-side displacement of the parallel excitation laser beams. Cambaliza and Saloma [19], Blanca and Saloma [21], Wang et al. [24] predicted and demonstrated that these constructed light techniques suppress background fluorescence generation. Lim and Saloma have predicted that error caused by spherical aberration is reduced with ND-2PE versus D-2PE [26]. Quentmeier et al. [27,28] demonstrated UV fluorescence lifetime measurements using ND-2PE in the visible spectrum, and Robinson et al. [29] demonstrated fluorescence lifetime imaging using ND-2PE combining visible and NIR wavelengths. Recently, Mahou et al. demonstrated that ND-2PE can be used for simultaneous excitation of four different fluorescent proteins in mouse cerebral cortex [30].

For the goal of deep penetration, ND-2PE holds a promise of attaining higher level of signals characteristic to D-2PE with deeper penetration typical for longer wavelengths of SWIR light. Specifically, we assume that one of the beams is chosen within the most “transparent” part of short-wavelength infrared (SWIR) optical window of ~1100-1400 nm or ~1600-1900 nm identified in a recent study [2,31]. ND-2PE can place the second beam within the ~700-1000 nm NIR wavelength range to supply the required photon energy for ND-2PE of visible emission fluorophores (green to red). The NIR beam will experience higher losses to scattering limiting the achievable power at the focal spot deep in the tissue. However, under ND-2PE, the emitted signal is proportional to the product of the power in each beam. Therefore, increasing the SWIR power will compensate for the NIR power due to scattering losses.

Chapter 2 starts with the theory of intermediate state resonance enhancement for supporting the enhancement of ND-2PE cross section. Many widely used fluorophores for brain images are introduced before we experimentally demonstrate the enhancement of ND-2PE cross section with some of these fluorophores. In addition, the ND-2PE system is described in details. In our experiments, we characterized beam overlap to ensure the accuracy of the measurement for ND-2PE cross section. The experimental results reveal the fact that detuning wavelength from the degenerated two-photon wavelength enhances the excitation cross section. Furthermore, we observed the signal enhancement from the image of eGFP tagged mice brain under ND-2PE and it was consistent with the spectroscopy results.

Chapter 3 presents a study in increased penetration depth with ND-2PE. At the beginning, a plot displays the attenuation length at different wavelengths in mice brain.

Degenerated two-photon microscopy is operated in a relatively high attenuated region while most of the three-photon microscopy is operated at the two transparent windows. ND-2PE involves two photons with different photon energies so that by introducing SWIR within one of the transparent window, the attenuation length can be effectively increased. The effect was demonstrated with our experiments and characterized based on Beer-Lambert law.

Chapter 4 investigates the reduction of out-of-focus excitation under ND-2PE with displaced beams. Out-of-focus excitation is this fundamental limit of brain image for degenerated two-photon microscopy and the phenomenon was elucidated and demonstrated in the literatures [9]. In our work, we designed an experiment to quantify the signal to background ratio (SBR) under D-2PE and ND-2PE. Afterwards, we examined the effects of displaced beams with fluorescent bead sample and demonstrated the ND-2PE with displaced beams can mitigate the background excitation. We also investigated the reduction of out-of-focus excitation in eGFP tagged mice brain.

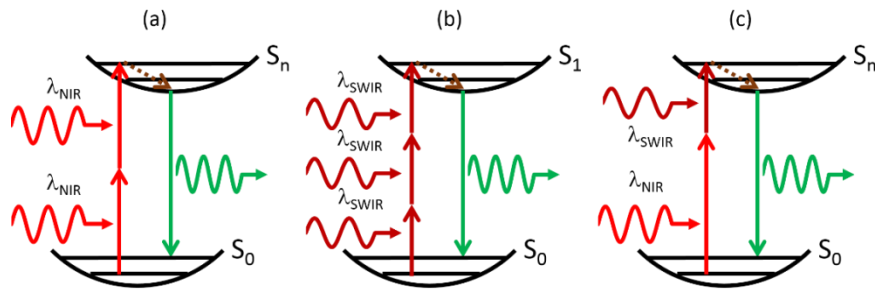


**Figure. 1.1.** Schematic energy diagram demonstrating degenerate and non-degenerate multi-photon absorption of a molecule: (a) degenerate 2-photon excitation (D-2PE); (b) degenerate 3-photon excitation (D-3PE); and (c) non-degenerate 2-photon excitation (ND-2PE).

# CHAPTER 2

## NON-DEGENERATED TWO PHOTON EXCITATION

ND-2PE is a process which involves two photons with different photon energies while D-2PE involves two photons with identical photon energy. Requirement for both mechanisms is the sufficient total photon energy to excite electrons from ground state to excited state. Therefore, an arbitrary wavelength combination can be chosen for ND-2PE as long as the photon energy fulfills the requirement and this mechanism provides more flexibilities in selecting the laser source and fluorophores. In fact, the detuned wavelength increases the excitation cross section due to ISRE. Consequently, ND-2PE generates fluorescence more efficiently than D-2PE and D-3PE. However, the price is the relatively complex system because the adjustment for the spatial and temporal overlap of two beams is necessary.

### 2.1 Background

Degenerate two-photon absorption / excitation (D-2PA/D-2PE) is a nonlinear process which involves two photons from the single light source. D-2PA has been attracting more attention in the field of silicon photonics, chemistry analysis and biology images in these decades [24,32,33]. For the application of biological images, two-photon excitation microscopy became a popular technique because of its two features: (1) high resolution

which originates from the quadratic dependence on the pump power (2) great penetration depth due to low attenuation at long wavelength. However, this mechanism is a low probability process and the short lifetime in the virtual state results in requiring high photon flux to excite electrons from ground state to excited state. Many groups have been putting effort on improving excitation efficiency by engineering the structure of the molecules [34]. The key was to bring the one-photon allowed state closer to the virtual state so that electrons' lifetime in the virtual state could be effectively elongated. The phenomenon is based on the theory of ISRE although this intuitive explanation is not correct in quantum physics. Unfortunately, the modified structures might lead to different optical properties as compared with the original molecules and these effects could not be excluded from the contribution of cross section enhancement. Joel M. Hales et al. [15] proposed to use two different laser sources (pump laser and one supercontinuum source generated from the same pump laser) for investigating the enhancement of excitation cross section without engineering molecules' structure. In their simulations and experiments, the total energy was kept constant and the increased excitation cross section directly resulted from ISRE. The improvement in their simulation was underestimated due to the discrepancy between excited state calculated from experimental data (single photon absorption measurement) and quantum-chemical calculation. However, the experimental results fairly match the theoretical predictions as they detuned the photon energy more from half of the bandgap. However, the enhancement of the excitation cross section for most of the fluorophores widely used in brain images have not been explored and this feature can achieve high brightness in images with lower excitation power in real application. Through chapter 2.2.2 to 2.2.4, the comprehensive analysis of ND-2PE study in fluorescent proteins and synthetic

fluorophores is presented. By varying energies of both photons, two-dimensional excitation landscapes were created in chapter 2.3. In chapter 2.3, the in vivo imaging in mouse brain (eGFP tagged) was also realized and the increase in image brightness was consisted with the spectroscopy findings.

## **2.2 Materials and Methods**

### **2.2.1 Fluorophores for Brain Image**

Figure 2.1 shows excitation cross section of many fluorophores for brain images with their excitation peaks from 700 nm to 1300 nm [35]. These fluorophores include organic, inorganic fluorophores and endogenous fluorescent proteins. While selecting fluorophores among different types of fluorophores, one would consider the optical and chemical properties such as excitation peak, brightness, photobleaching, and PH range sensitivity. Currently, Brain Initiative Community is seeking for synthesized red fluorophores with high excitation cross section since the longer excitation and emission wavelength can push the penetration length deeper in brain tissues. We would expect that there will be few studies in red fluorophores with the excitation wavelength between 1300 nm and 1500 nm because the excitation wavelength is within strong water absorption band. However, if there exists this kind of fluorophores in the future, ND-2PE can solve this problem by placing two wavelengths outside strong water absorption region and efficiently excite the fluorophores.

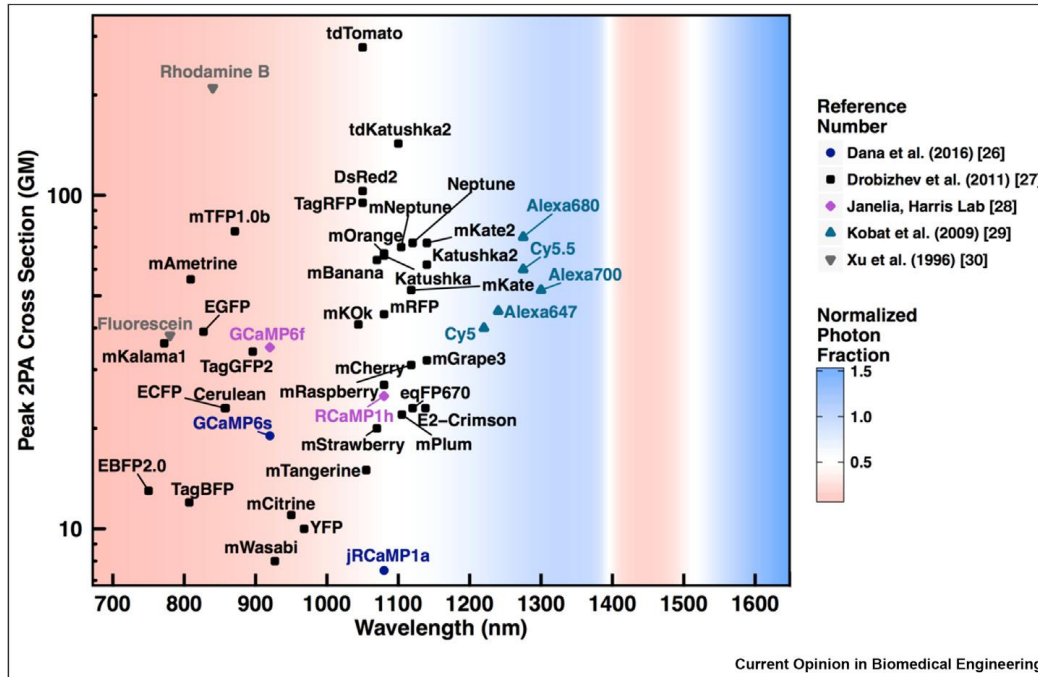


Figure 2.1: Widely used fluorophores in brain images (Excitation wavelength from 700 nm to 1300 nm)

## 2.2.2 Non-degenerated Two Photon Excitation Setup

We designed a non-degenerated two-photon system for ND-2PE spectroscopy shown in Fig. 2.2. Ultrashort pulses were derived from a Ti:Sapphire laser (Coherent Chameleon Ultra II, tuned from 740 nm or 870 nm; further referred to as the NIR beam) and an optical parametric oscillator (Chameleon Compact OPO, tuned from 1000 nm to 1400 nm; further referred to as the SWIR beam). According to the tuning range of the laser system, the wavelength combinations of ND-2PE have equivalent D-2PE wavelengths between 850 nm and 1073 nm. (The tuning range and output power of Chameleon-OPO system is shown supplementary materials. The SWIR wavelength from OPO system is determined by the optics design and optical properties of nonlinear crystal in the system.)

The partial NIR beam was launched into the OPO and generated synchronized SWIR beam. A delay line (Thorlabs LTS150) with a resolution of 2  $\mu\text{m}$ , which is temporally equivalent to 6.6 fs, was used to temporally overlap the NIR and the SWIR laser pulses. A computer code (Matlab) was devised to automate the temporal overlap of the NIR and SWIR pulses by scanning the delay line and logging PMT readings at each position. Several lenses and mirrors in each optical path were used to adjust spatial overlap of the NIR and SWIR laser as indicated in Fig. 2.2. These two laser beams were combined by a dichroic mirror (Thorlabs, DMSP 1000) before the detection part. The two overlapping and collinear beams were focused by a microscope objective lens (Newport, 5712-A-H 40X) into the sample, which also collected the emitted fluorescence signal in epi-illumination. In order to detect fluorescence, two dichroic mirrors (Semrock, FF678-Di01-25x36 and FF735-Di01-25x36) and a bandpass filter were placed in front of a photomultiplier tube (PMT, Hamamatsu R3896) with which the fluorescence was detected.

To take neuron images in mice brain, we built a homemade microscope by referring to [36] (Fig.2.3 and Fig.2.4 (a,b)). In addition to focusing the laser beams, the microscope objective lens (Olympus, UMPlanFLN 20X/0.5) was used to collect the emitted fluorescence signal in epi-illumination scheme. In order to efficiently collect fluorescence signal while taking the images, two dichroic mirrors with 2-inch in diameter (Thorlabs, DMLP650L), two achromatic lenses (Thorlabs, AC508-400-A-ML and Edmunds, #48-660) and two bandpass filters (Semrock, FF01-550/200-25) were placed in front of the photomultiplier tube (PMT, Hamamatsu H11461-01) with which the fluorescence was detected. Moreover, a signal amplifier and an electrical low pass filter were added between the PMT and the DAQ card to improve the signal to noise ratio. Instead of scanning two

laser beams with Galvo mirror system, we translated the sample on three one-dimensional translation stages (PI, 110.1DG) with the step size of 40 nm. The fluorescent signal was recorded at every position in three axes by synchronizing the encoders of the translation stages and the DAQ card output. The entire microscope was enclosed with optical enclosures (Thorlabs, XE25C10) to further isolate the system from the ambient noise.

We characterized spatial overlap of the two beams and the beam size at focal plane by using the method described in [37]. In addition, we verified that optimizing the fluorescence signal could guarantee good spatial overlap of NIR beam and SWIR beam with an experiment described in the supplementary materials. In the experiment, we used knife-edge method at three different axial planes after the focal plane and located the center of NIR beam and SWIR beam. From this measurement, we also could calculate the spot size at focus.

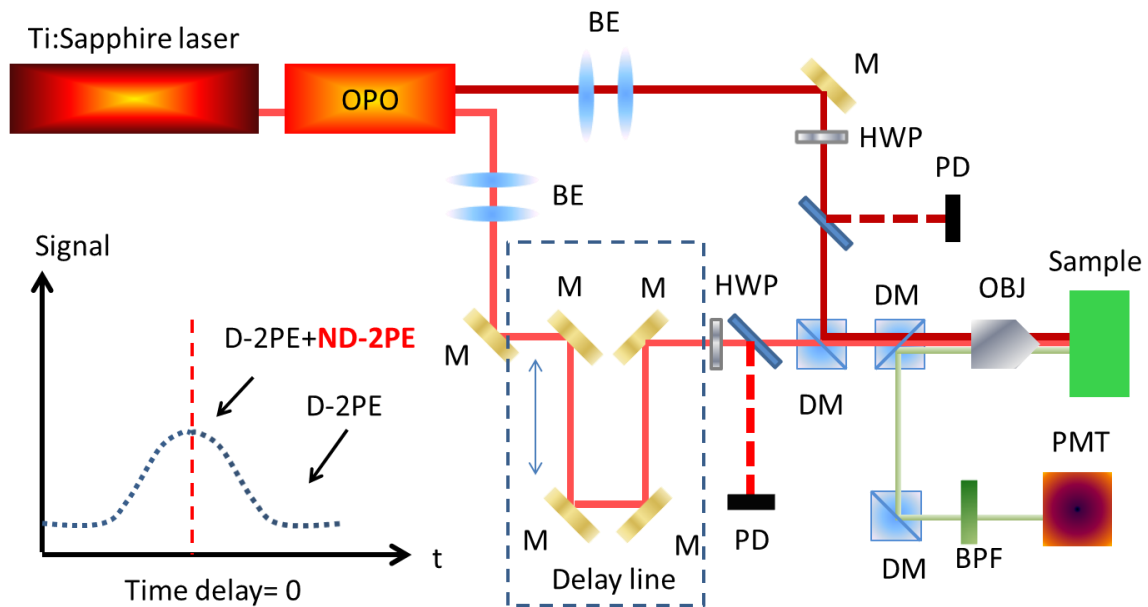


**Figure 2.2:** Spectroscopy setup of ND-2PE. HWP, half wave plate; DM, dichroic mirror; BE, beam expander; PD, photodetector; M, mirror; PMT, photon multiplier tube; BPF, bandpass filter.

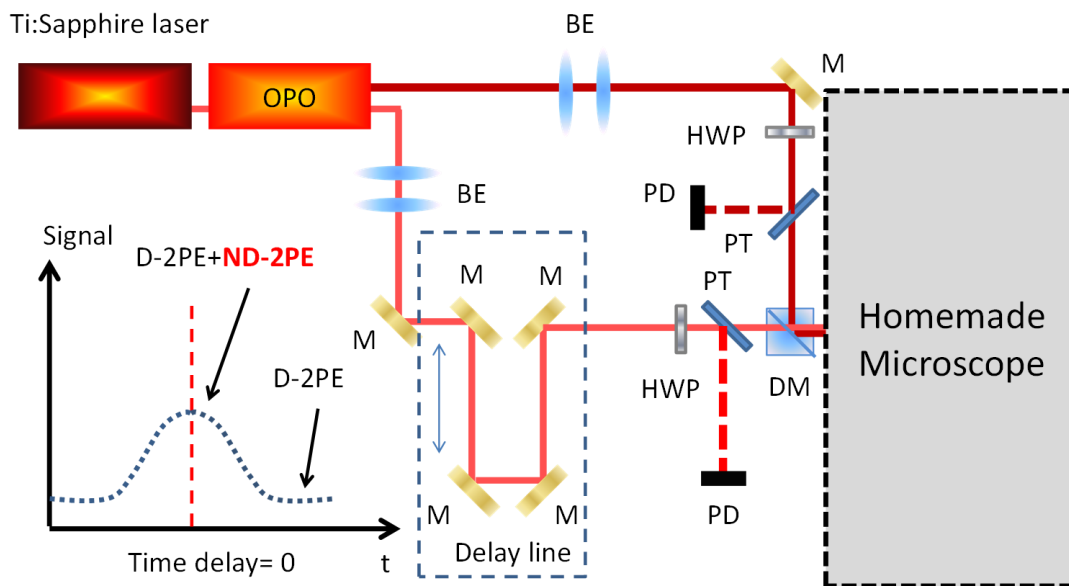


**Figure 2.3:** ND-2PE microscope. HWP, half wave plate; DM, dichroic mirror; BE, beam expander; PD, photodetector; M, mirror; PMT, photon multiplier tube; PT, Photon taper.

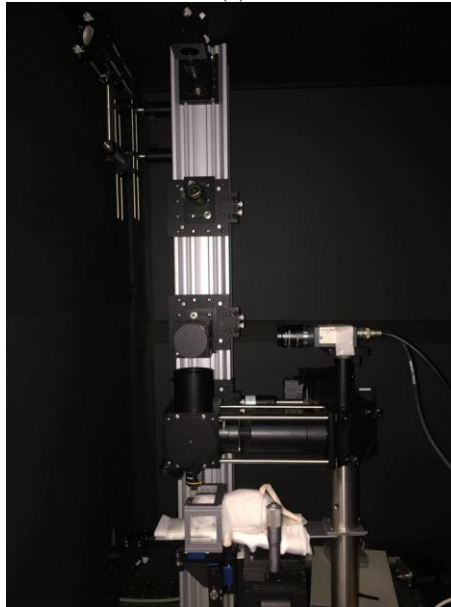
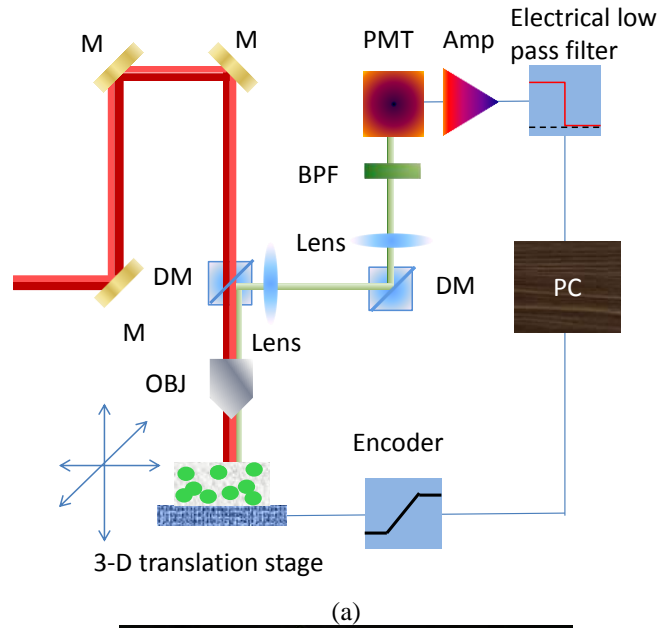


**Figure 2.4:** (a) Layout of the homemade microscope. M, mirror; DM, dichroic mirror; OBJ, 20X microscope objective; BPF, band pass filter; PMT, photomultiplier; Amp, signal amplifier (b) Real system with a fake mouse.

### 2.2.3 Fluorescence Generation with Beam Overlap

First, we investigated the dependence of the fluorescence signal on the temporal alignment [Fig. 2.5(a)] and photon flux of each beam [Figs. 2.5(b,c)] in a transparent

medium (500  $\mu$ M fluorescein in saline). The temporal alignment was optimized by scanning the optical delay line, and the fluorescence signal was detected by the PMT. Irrespective of the delay line position, we observed a fluorescence signal generated by the D-2PE due to the NIR excitation [Fig. 2.5(a), “D-2PE”]. No fluorescence signal was generated under D-2PE with the SWIR beam alone because of its insufficient photon energy for fluorescein [38]. An increase in the fluorescence signal was detected as the two beams overlapped indicating the additive effect of the ND-2PE occurring due to the simultaneous absorption of NIR and SWIR photons [Fig. 2.5(a), “D-2PE + ND-2PE”]. This additive property indicated that, under our experimental conditions, depletion of the NIR beam due to its absorption by the fluorophore in the D-2PE regime was insignificant. For the experiments in this section, the NIR beam wavelength was 825 nm and the SWIR wavelength was 1315 nm. For spectroscopy measurement in the following sections, we swept both wavelengths.

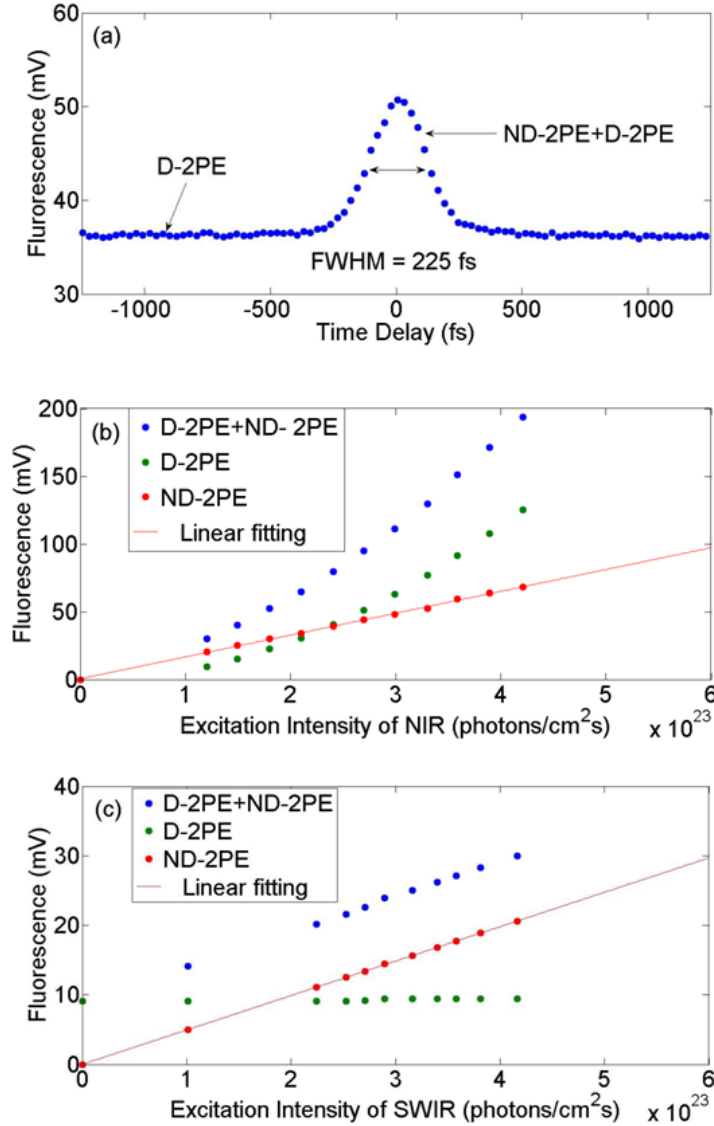


**Figure 2.5:** Experimental demonstration of ND-2PE. (a) dependence of the fluorescence signal on temporal alignment; (b) fluorescence intensity dependence on NIR power (SWIR intensity is fixed at  $4.16 \times 10^{23}$  photons/cm<sup>2</sup>s); (c) fluorescence intensity dependence on SWIR power (NIR intensity is fixed at  $1.18 \times 10^{23}$  photons/cm<sup>2</sup>s).

Next, we examined the dependence of the fluorescence signal on the power of each beam [Figs. 2.5(b) and 2.5(c)]. In the absence of SWIR excitation the signal scaled quadratically with the NIR power (green curve in Fig. 2.5(b)), which confirms D-2PE of the sample with 825nm excitation [39]. With both lasers illuminating the sample, the

fluorescence signal increased with an increase in power of each beam. In Fig. 2.5(b) the SWIR intensity was held constant and in Fig. 2.5(c) the NIR intensity was held constant. By subtracting the D-2PE fluorescence contribution [Figs. 2.5(b,c), green curves] from the fluorescence measured with simultaneous degenerate and non-degenerate excitation [Figs. 2.5(b,c), blue curves] we obtained the ND-2PE fluorescence contribution [Figs. 2.5(b,c), red curves]. As expected, the ND-2PE signal increased linearly in both experiments [37]. The measured power dependences in Fig. 2.5(c) do not start from zero because of the fluorescence due to D-2PE at the fixed NIR power. A cubic dependence of the fluorescence intensity with changing SWIR intensity due to 3-photon excitation was not observed due to insufficient SWIR power (emphasizing the low efficiency of 3PE compared with ND-2PE) [40]. Thus, we have confirmed that our choice of NIR and SWIR wavelengths result in both D-2PE and ND-2PE of our fluorescein sample. After verifying the power dependence of the fluorophore, we analyze and measure ND-2PE cross section in next section.

#### 2.2.4 Non-degenerated Two Photon Excitation Cross Section

To create a model of the fluorescence generated by the absorption of two photons of different energy we begin with the same assumptions as Xu and Webb [38]: we assume that there is an absence of stimulated emission, photo-bleaching and saturated absorption. Thus, the fluorescence photon flux is

$$F(t) = \phi\eta N_{abs}, \quad (1)$$

where  $\phi$  is the collection efficiency of the optical system,  $\eta$  is the fluorescence quantum efficiency and  $N_{abs}$  is the number of absorbed photons per unit time. We have

dropped the factor of one half because the number of absorbed photons contains the non-degenerate two photon absorption.

To extend  $N_{abs}$  to include non-degenerate absorption, we assume that both the NIR and SWIR excitation beams are undepleted for all time and relative pulse delays:

$$N_{abs}(t) = N_{abs}^{ND}(t, \tau) + 1/2 N_{abs}^{NIR}(t) + 1/2 N_{abs}^{SWIR}(t), \quad (2)$$

where,  $N_{abs}^{ND}$  is the non-degenerate absorption term, and  $N_{abs}^{NIR}$  and  $N_{abs}^{SWIR}$  represent the degenerate 2-photon absorption of the NIR and SWIR beams, respectively, and  $\tau$  is the temporal offset between NIR and SWIR beams. The derivation of the degenerate absorption terms proceeds identically to that ref. [38], so the remaining analysis will focus on the ND term.

The number of absorbed photons per unit time in the non-degenerate case is

$$\begin{aligned} & N_{abs}^{ND}(t, \tau) \\ &= 4 \int_V dV \sigma_{ND}^{(2)}(\lambda_{NIR}, \lambda_{SWIR}) C(\mathbf{r}, t) I_{NIR}(\mathbf{r}, t, \tau) I_{SWIR}(\mathbf{r}, t), \end{aligned} \quad (3)$$

where  $\sigma_{ND}^{(2)}$  is the non-degenerate 2-photon absorption cross section,  $\lambda_{NIR}$  and  $\lambda_{SWIR}$  are the wavelengths of the NIR and SWIR beams,  $C(\mathbf{r}, t)$  is the temporal and spatial dependent distribution of the fluorophore concentration, and  $I_{NIR}$  and  $I_{SWIR}$  are the time and space dependent photon fluxes of each beam. The factor of four is from the nonlinear interaction of two electrical fields (NIR and SWIR beams). Under the assumption that the fluorophores are distributed homogeneously and are stable over the course of each measurement (in addition to the previously mentioned assumptions) the concentration is constant, i.e.,  $C(\mathbf{r}, t) = C$ , and can therefore be removed from the integral:

$$N_{abs}^{ND}(t, \tau) = 4\sigma_{ND}^{(2)} C \int_V dV I_{NIR}(\mathbf{r}, t, \tau) I_{SWIR}(\mathbf{r}, t). \quad (4)$$

Subsequently, we approximate each beam as a Gaussian pulse with a Gaussian cross section, in the paraxial approximation, which allows us to separate the temporal and spatial components of the photon flux:

$$\begin{aligned} I_{SWIR}(\mathbf{r}, t) &= S_{SWIR}(\mathbf{r}) T_{SWIR}(t), \\ I_{NIR}(\mathbf{r}, t) &= S_{NIR}(\mathbf{r}) T_{NIR}(t - \tau), \end{aligned} \quad (5)$$

where the foci of each beam are assumed to be overlapped in space, and

$$\begin{aligned} T(t; \lambda) &= I_0^{(\lambda)} \exp\left(\frac{-t^2}{2\Gamma_\lambda^2}\right), \\ S(\mathbf{r}; \lambda) &= \left[\frac{w_0(\lambda)}{w(z; \lambda)}\right]^2 \exp\left[-2\left(\frac{r}{w(z; \lambda)}\right)^2\right], \end{aligned} \quad (6)$$

where  $r$  is the radial distance from optical axis, the beams are assumed to be transform limited pulses with peak photon flux density  $I_0^{(\lambda)}$  and temporal standard deviation  $\Gamma(\lambda)$ , and

$$\begin{aligned} w^2(z; \lambda) &= w_0^2(\lambda) \left[1 + \left(\frac{z}{z_0(\lambda)}\right)^2\right], \\ z_0(\lambda) &= \frac{\pi w_0^2(\lambda)}{\lambda}, \quad w_0 = \frac{\lambda}{\pi NA} \end{aligned} \quad (7)$$

where  $w_0(\lambda)$  is the beam waste of the excitation beam of wavelength  $\lambda$  [39]. Inserting these expressions into Eq. (4) and separating the spatial and temporal terms we find

$$N_{abs}^{ND}(t, \tau) = 4\sigma_{ND}^{(2)}C[T(t; \lambda_{SWIR})] \int_V dV S(\mathbf{r}; \lambda_{NIR})S(\mathbf{r}; \lambda_{SWIR}) \quad (8)$$

By assuming the fluorescence spot size is much smaller than the volume of the fluorophore solution and the numerical apertures of each beam are roughly equal, the spatial overlap integral evaluates to

$$\int_V dV S(\mathbf{r}; \lambda_{NIR})S(\mathbf{r}; \lambda_{SWIR}) \approx \frac{1}{2\sqrt{2}} \frac{1}{\pi NA^4} \frac{(\lambda_{NIR}\lambda_{SWIR})^2}{\sqrt{\lambda_{NIR}^2 + \lambda_{SWIR}^2}}, \quad (9)$$

where NA is the numerical aperture of the optical system.

As in [38], we recognize that the signal measured by our fluorescence detector is the time averaged photon flux, not the instantaneous photon flux; as a result, we compute the time average of Eq. (1):

$$\langle F(t) \rangle = \frac{2}{\sqrt{2}} \frac{\phi[\eta \sigma_{ND}^{(2)}]C}{\pi NA^4} \frac{(\lambda_{NIR}\lambda_{SWIR})^2}{\sqrt{\lambda_{NIR}^2 + \lambda_{SWIR}^2}} \left\{ f \int_{-1/2f}^{1/2f} dt' T(t'; \lambda_{SWIR})T(t' - \tau; \lambda_{NIR}) \right\}, \quad (10)$$

where  $f$  is the laser repetition rate and the combined terms  $\eta\sigma_{ND}^{(2)}$  are called the non-degenerate action cross section, to distinguish this quantity from the absorption cross section. If we assume the pulse width and delay time are much smaller than  $1/f$ , which is valid for an 80 MHz femtosecond pulsed laser, we can approximate the limits of this integral to be infinite:

$$\begin{aligned}
& \int_{-1/2f}^{1/2f} dt' T(t'; \lambda_{SWIR}) T(t' - \tau; \lambda_{NIR}) \\
& \approx \int_{-\infty}^{\infty} dt' T(t'; \lambda_{SWIR}) T(t' - \tau; \lambda_{NIR}).
\end{aligned} \tag{11}$$

This expression is equivalent to the temporal convolution of our laser pulses. Substituting Eq. (6) into (11) we see that as a function of delay time, we have the convolution of two Gaussian functions, which is typically computed by application of the convolution theorem:

$$f * g = \mathcal{F}^{-1}\{\mathcal{F}\{f\} \cdot \mathcal{F}\{g\}\}, \tag{12}$$

where  $f * g$  denotes the convolution of functions “ $f$ ” and “ $g$ ” and  $\mathcal{F}\{\cdot\}$  is the Fourier transform. Therefore, the temporal convolution of our Gaussian pulses is

$$\begin{aligned}
& \int_{-\infty}^{\infty} dt' I_0^{(NIR)} I_0^{(SWIR)} \exp\left(\frac{-(t' - \tau)^2}{2\Gamma_{NIR}^2}\right) \exp\left(\frac{-t'^2}{2\Gamma_{SWIR}^2}\right) \\
& = \sqrt{2\pi} I_0^{(NIR)} I_0^{(SWIR)} \frac{\Gamma_{NIR} \Gamma_{SWIR}}{\Gamma_x} \exp\left(\frac{-\tau^2}{2\Gamma_x^2}\right),
\end{aligned} \tag{13}$$

where  $\Gamma_x^2 = \Gamma_{IR}^2 + \Gamma_{SWIR}^2$  is the standard deviation of the convolution.

To complete the derivation, we rewrite the time averaged fluorescence in terms of the average laser power. Because we assumed transform limited Gaussian pulses with a Gaussian spatial profile, we can write the power in terms of the photon flux

$$\langle P_\lambda \rangle = I_T E_\lambda f \tag{14}$$

where  $I_T = \int I_\lambda(\mathbf{r}, t) d\mathbf{r} dt$ , is the total photon flux,  $E_\lambda$  is the energy per photon, and  $f$  is the number of laser pulses per unit time. Consequently, we obtain the following equation for the laser photon flux

$$I_0^{(\lambda)} = \frac{2 \lambda \langle P_\lambda \rangle}{\sqrt{2\pi} \Gamma c h f \pi w_0^2} = \frac{\sqrt{2\pi} NA^2 \langle P_\lambda \rangle}{\Gamma c h f \lambda}, \quad (15)$$

where  $c$  is the speed of light,  $h$  is Plank's constant and  $\langle P_\lambda \rangle$  is the average power as measured on a power meter. Therefore, assuming: the fluorophore solution is homogeneous; the paraxial beam approximation; an approximately constant numerical aperture; transform limited Gaussian pulses; and, undepleted excitation beams, the time averaged photon flux as a function of relative pulse delay is

$$\begin{aligned} & \langle F(\tau) \rangle_{ND} \\ & \approx \frac{4 \sqrt{\pi} C \langle P_{NIR} \rangle \langle P_{SWIR} \rangle}{f c^2 h^2} \frac{\lambda_{NIR} \lambda_{SWIR}}{\sqrt{\lambda_{NIR}^2 + \lambda_{SWIR}^2}} \frac{[\phi \eta \sigma_{ND}^{(2)}]}{\Gamma_x} \exp\left(\frac{-\tau^2}{2\Gamma_x^2}\right). \end{aligned} \quad (16)$$

Furthermore, by recognizing that the total fluorescence,  $\langle F(\tau) \rangle$ , results not only from non-degenerate excitation, but also degenerate excitation, which is constant as a function of pulse delay, we can use the baseline offset of the convolution signal to acquire the degenerate action cross section as well, i.e.,

$$\langle F(\tau) \rangle = \langle F(\tau) \rangle_{ND} + \langle F \rangle_D. \quad (17)$$

To perform ND-2PE spectroscopy with the above equations, the experimental conditions and required parameters are described as the following. The measurement was conducted by sweeping the wavelength of NIR beams (from 740 nm to 870 nm) with Ti:Sapphire laser and IR beams (from 1000 nm to 1400 nm) with synchronized optical parametric oscillator (OPO). Both beams were temporally and spatially aligned and co-polarized. The step size for wavelength sweep was 10 nm. Based on the recorded average power, central wavelength, spectral pulse width, and spot size at each wavelength, the two-

dimensional ND-2PE spectroscopy can be obtained. The calculation relied on fitting the profile of fluorescent signal at different time delay with Eq. (16). In addition, D-2PE spectroscopy can be obtained from either individual D-2PE measurement or from the fluorescence signal generated by NIR beam in the ND-2PE experiment. To emphasize the enhancement of ND-2PE cross section, all the data points in 2D map of ND-2PE spectroscopy were normalized by the peak cross section in D-2PE spectrum. All measurements were conducted at sufficiently low incident power to avoid photobleaching and pump depletion.

### 2.3 Results

ND-2PE spectroscopy of three fluorescent proteins (eGFP, MKO2, and mCerulean) and two synthetic dyes (fluorescein and Cumarin) was performed using a setup described in Fig. 2.2. The independently measured cross sections  $\sigma_D^{(2)}$  (blue curve, left column of Fig. 2.6) were consistent with the D-2PE measurement extracted from ND-2PE experiment (black curve, left column in Fig. 2.6) and the data points of the excitation peaks were used for normalizing the ND-2PE cross section (right column in Fig.2.6). The D-2PE spectrum extracted from ND-2PE measurement was from 740 nm to 870 nm since only the pump wavelengths within this range could generate SWIR beams from our OPO system. The right column in Fig 2.6 depicts the normalized  $\sigma_{ND}^{(2)}$  with different wavelength combination. The data points in the 2-D map were also converted to the equivalent D-2PE wavelengths and were plot as red dots in the left column in Fig 2.6. Along an isocline (a vertical line at any wavelength), multiple wavelengths combinations sum up to the same total energy. The NIR beam with higher photon energy along isocline gives greater enhancement and this

result supports the theory of ISRE. In all the examined cases, we observed enhancement of ND-2PE cross section, up to ~1.5 fold (comparison between blue curve and red dots). It is noticeable that there exist few discontinued data points in the 2D plot since the OPO system produced double-peak pulses at few wavelengths and it led to uncorrected curve fitting of the fluorescent signal at different time delay. To verify the accuracy of our experiment, we compared the D-2PE spectroscopy of two fluorescent proteins with the reported data in the literatures which are list in supplementary figures.

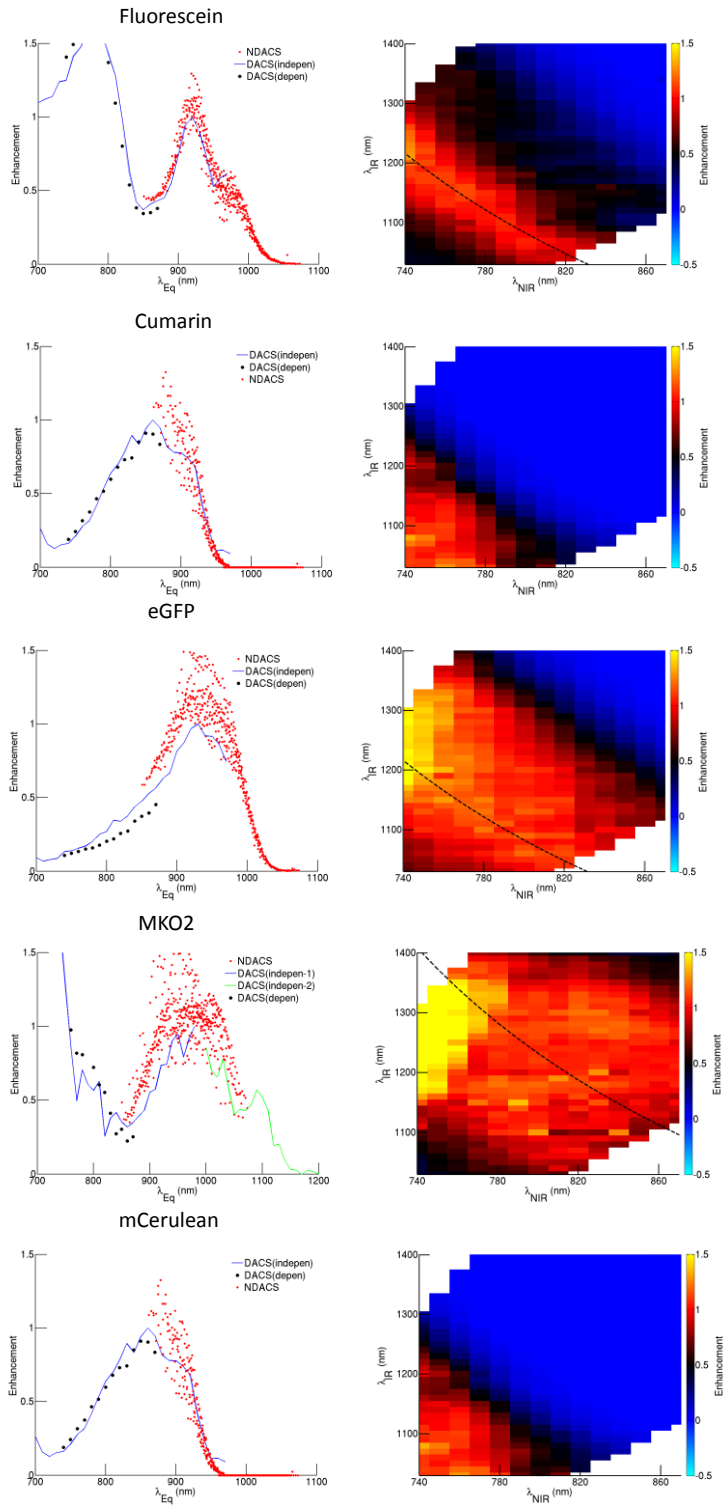
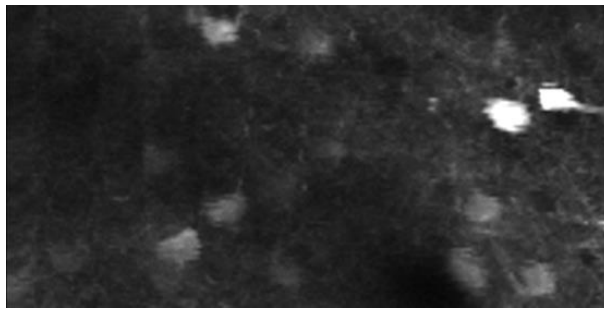
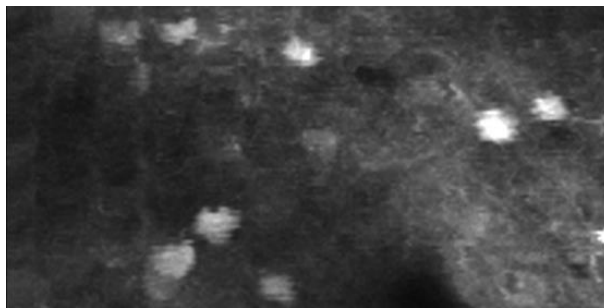


**Figure 2.6:** ND-2PE spectrum for fluorophores (fluorescein, Cumarin, eGFP, MKO2, and mCerulean,)

To investigate the performance of ND-2PE in the real application, an image experiment with an eGFP tagged mouse was conducted. The NIR wavelength and SWIR wavelength in this experiment was 740 nm and 1230 nm, respectively and pump laser at 920 nm was also used to generate D-2PE images for the comparison purpose. Fig. 2.7 (a) is the D-2PE image and Fig 2.7 (b) is the ND-2PE image at the depth of 200  $\mu\text{m}$ . Fig. 2.8 shows the histogram of the fluorescence signal in these images. We calculated the excitation photon flux according to the optical parameters mentioned in chapter 2.2.4. By pumping the same excitation photon flux onto the neurons, the fluorescent signal was enhanced by factor of 1.5 which was close to the spectroscopy measurement. The mount system for the mice head is described in supplementary materials.



(a)



(b)

**Figure 2.7:** Images of eGFP tagged mice brain under (a) D-2PE (b) ND-2PE

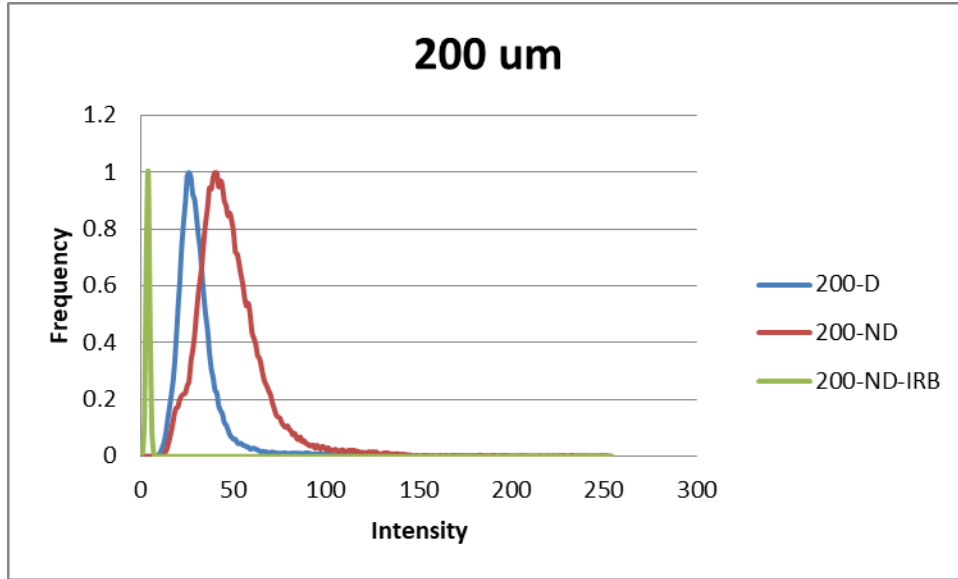


**Figure 2.8:** The histogram of the fluorescence signal under D-2PE and ND-2PE at the depth of 200  $\mu\text{m}$ .

## 2.4 Discussion

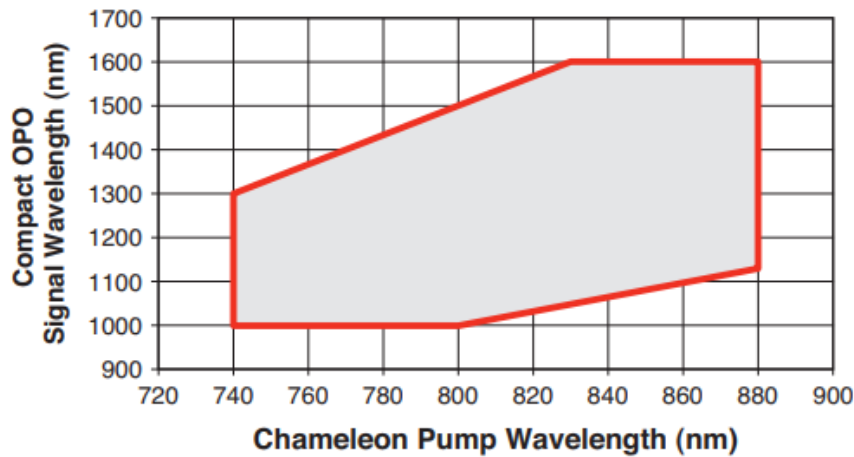
The theory of ISRE predicts greater two-photon absorption cross section if one of the photon energies is tuned close to the lowest one-photon allowed state. In this work, the tuning range was limited by the Chameleon-OPO system so that the significant enhancement could not be achieved. Theoretically, it is still possible to pump red fluorophores with one beam from Ti:sapphire laser (740 nm to 880 nm) and the other beam from the idler output of OPO system (1680 nm to 5000 nm) and these wavelength combination can give more enhancement. However, most of the commercial optics do not satisfy the requirement of minimum chromatic dispersion and aberration with this wide wavelength range. In fact, even if the significant enhancement can be achieved by a laser system with arbitrary tuning range, the effect is limited by the attenuation in brain tissues. Nevertheless, the enhancement of ND-2PE cross section helps to increase the image

brightness and it provides some degrees of freedom in selecting wavelength combination from laser source for a specific fluorophore.

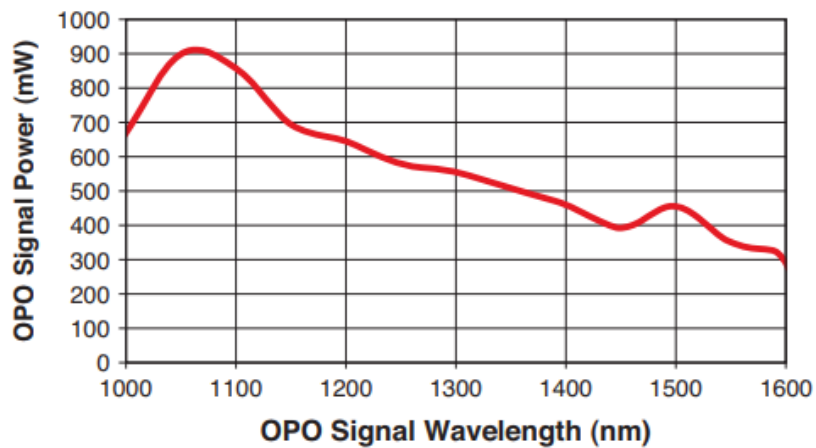
The demonstration of the signal enhancement with eGFP tagged the mouse brain supported the spectroscopy results but the experimental condition was not optimized due to the degradation of beam overlap from the scattering in the brain tissues. Not only the spatial walk-off but also the wave-front distortion deteriorated the beam overlap. This implies that it is inevitable to apply adaptive optics to our system although it would increase the complexity of the system and introduce extra loss. Conventionally, people recorded the phase of scattered pump beams and constructed a feedback loop to precompensate phase distortion. ND-2PE allows to use the SWIR beam as “guiding star” for correcting the phase of NIR beam by optimizing the fluorescence signal and this is a relatively simple system. In this experiment, the temporal walk-off due to the chromatic dispersion was a minor issue since the beams only penetrated few hundred microns into brain tissues and the effect was verified by scanning the optical delay line at different depths. When excitation photons penetrate up to one millimeters, the estimated time delay between two pulses are around 40 femtoseconds if the dispersion is mainly from water.

## 2.5 Supplemental Materials

Fig. 2.9 shows the tuning range of Chameleon-OPO system and the output power of the signal from OPO. These two plots are referred to the manual on the website of Coherent, Inc. The performance of the system is slightly different for individual lasers. In our system, the longest wavelength of NIR beam that can generate signal output from OPO was 870 nm.



(a)



(b)

**Figure 2.9:** (a) The tuning range of Chameleon-OPO system (b) The power of signal output from OPO

In our spectroscopy experiment, we spatially aligned two beams by optimizing fluorescence signal with the mirrors and the defocuser in the IR path. After that, we temporally aligned two beams with the optical delay line. Iterative adjustments for spatial overlap and temporal overlap were conducted until fluorescence signal was maximized. To verify that the optimal beam overlap could be guaranteed in this way, we resolved the intensity distribution of the NIR beam and IR beam with knife edge method at different axial planes. The setup is illustrated in Fig. 2.10 and the NIR wavelength and IR wavelength was set to 740 nm and 1230 nm, respectively. The lens was the same lens used in the experiments in chapter 2.3. As shown in Fig. 2.11, the intensity of NIR beam and IR beam clipped by a blade were measured by a photodetector and we fit the curve with standard error function. Table 2.1 summarizes the center position of the NIR beam and IR beam and it shows some negligible shifts which is within the experimental error. In addition, we also confirmed the axial alignment by profiling the fluorescence signal with an 1- $\mu\text{m}$  thick fluorescein sample at different axial positions. The result is plotted in Fig. 2.11.

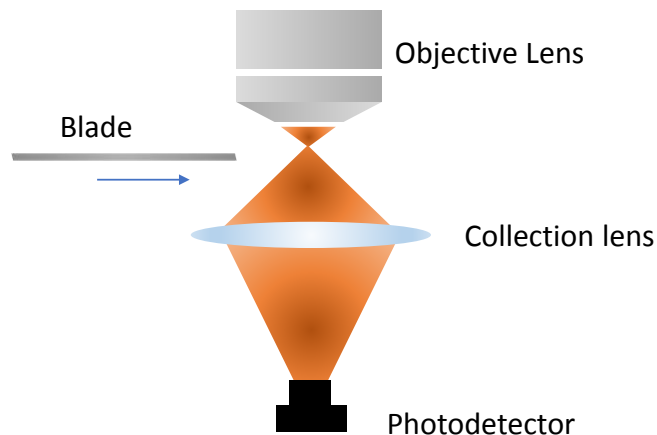


**Figure 2.10:** Experimental setup for resolving the intensity distribution of NIR beam and IR beam

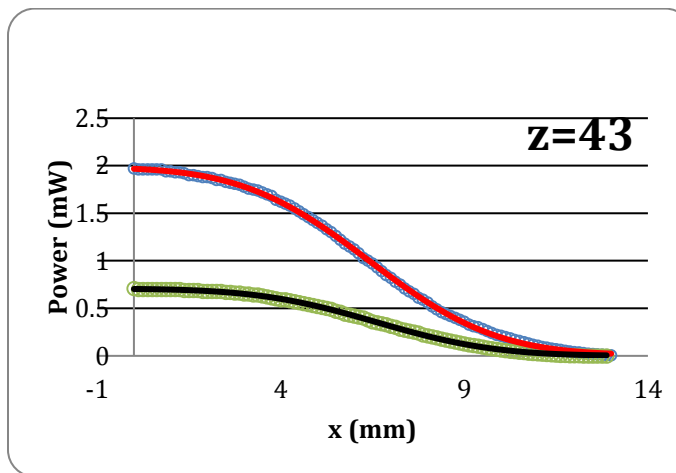
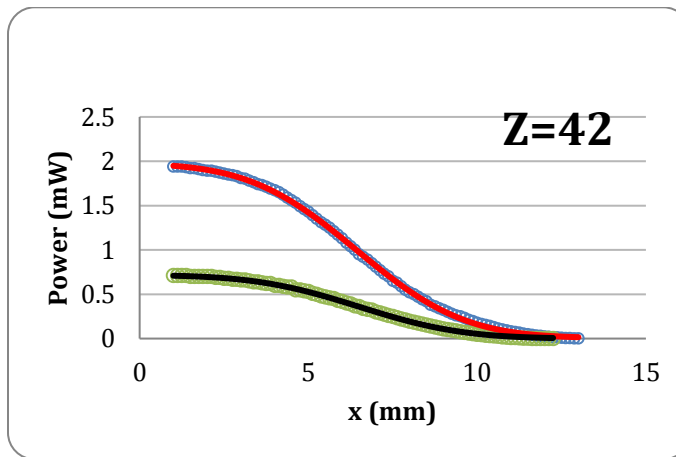
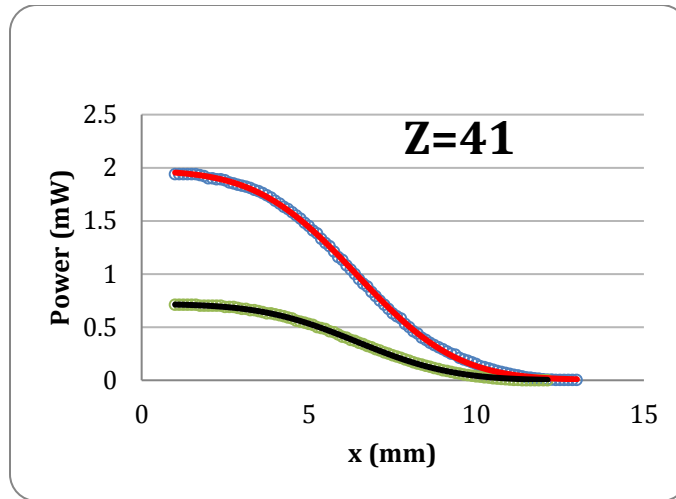


**Figure 2.11:** Intensity distribution of NIR beam (green curve) and IR beam (red curve) at different axial planes.

**Table 2.1:** Summary of the center position of the NIR beam and IR beam at different axial planes.

	Axial position 1 Z=41 mm from a reference plane	Axial position 2 Z=42 mm from a reference plane	Axial position 3 Z=43 mm from a reference plane
740 nm	6.43 mm	6.45 mm	6.52 mm
1230 nm	6.44 mm	6.50 mm	6.60 mm

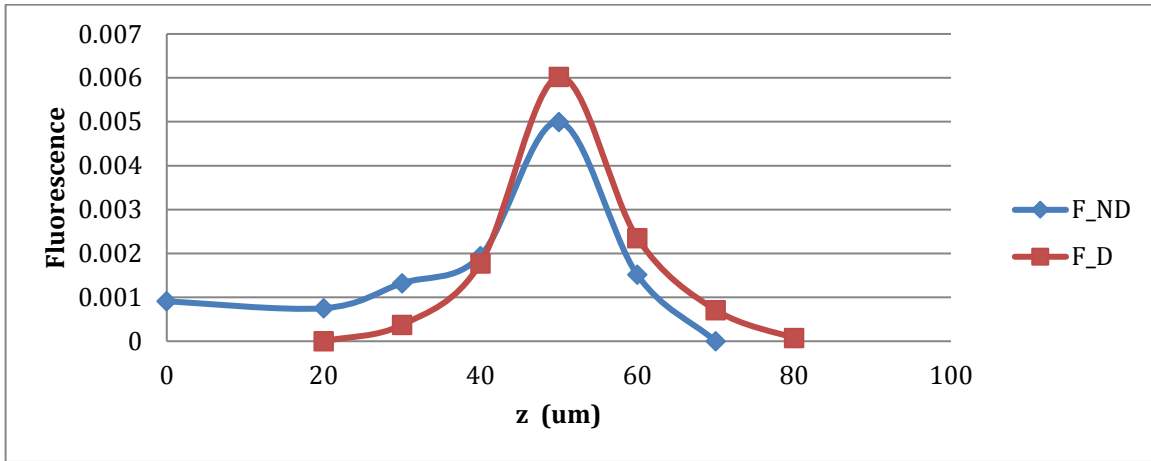
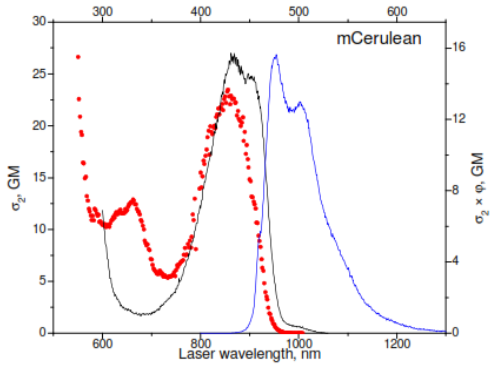
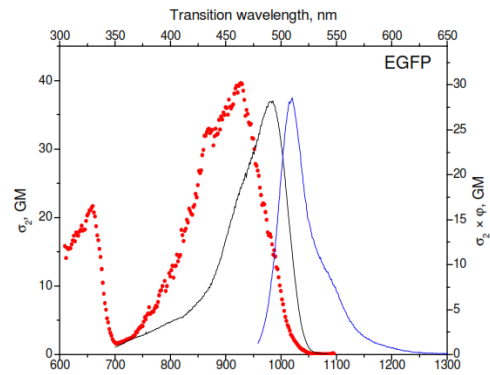


**Figure 2.12:** Fluorescence signal under D-2PE (red curve) and ND-2PE (blue curve) at different axial position.

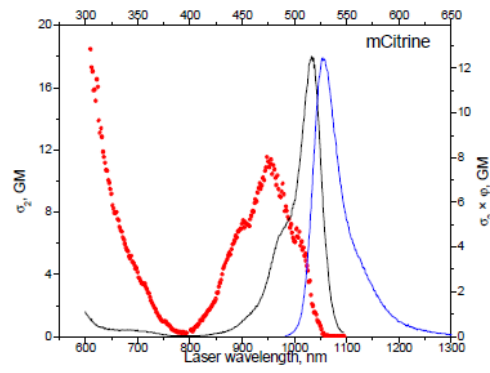
To ensure our measurement for D-2PE spectroscopy was accurate, we compared our D-2PE measurement with the reported data [41] shown in Fig.2.13 (a,b). In our experiment we did not measure the absolute excitation cross sections but the relative value could be used to compare with the reported data. Fig. 2.14 (c) shows the D-2PE spectrum of one fluorescent protein we plan to measure in the future.



(a)



(b)



(c)

**Figure 2.13:** The D-2PE spectrum for fluorophores reported in the literatures.

The preparation of the mice is described as following. A costumer holding and cranial window, from either craniotomy or skull thinning, allowing cranial access and repeated head immobilization was implanted under general anesthesia prior to imaging. The cranial window was covered with a round glass coverslip and sealed with dental acrylic. At the beginning, we did a preliminary imaging experiment one to two hours after the surgery. It took one to three weeks for mice to recover from the surgery. In order to make mice accustomed to long period experiment with head restrain, mice were habituated in 1 session per day to accept increasingly longer periods: 15-120 min per session. During the head restraint, we needed to make sure mice was not overreacting by torquing the body. The head fixation procedure was not painful and trained animals did not show signs of distress. They display grooming behavior from time to time and fall asleep in the absence of external stimuli. (e.g., air puff to the whiskers.) This type of experiment in awake head fixed mice was exercised widely around the world including a number of labs here at UCSD.

The mount system for mice heads is shown in Fig. 2.14. We put mice on a long plate while the head mount was moving with the translation stages. A warming pad was inserted between mice and the long plate to keep the body temperature as mice were sleeping. Since the scanning distance of the translation stage was less than 1 mm and the mice heads were fixed on a solid mount, no drifting of the images was observed. To evaluate the drifting in every line scan, we tested the system with 1- $\mu$ m bead sample. An image of perfect circular beads indicated that there was no noticeable jitter from the translation stages.

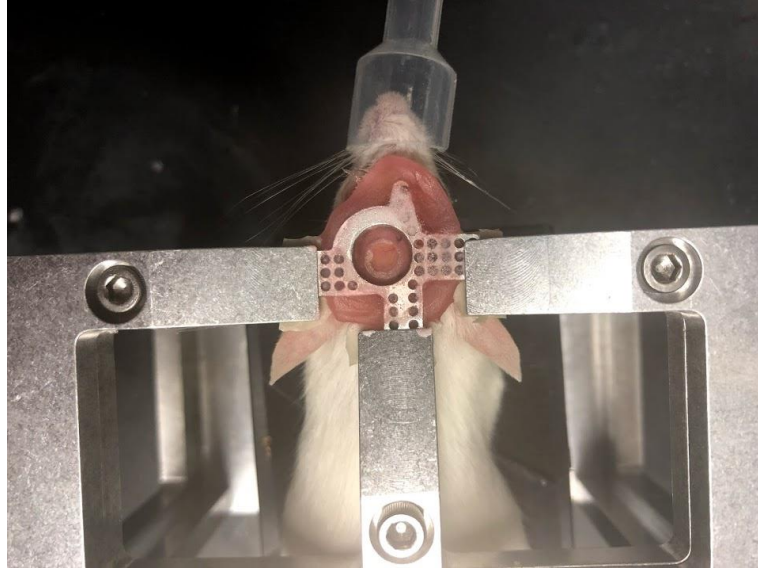


**Figure 2.14:** Mount system for mice heads.

## **Acknowledgements**

Chapter 2 covers the work of non-degenerate 2-photon microscopy which demonstrate the enhancement of excitation cross section. Chapter 2, in part is currently being prepared for submission for publication of the material. Chris Ferri; Mu-Han Yang; Sanaz Sadegh; Martin Thunemann; Payam Saisan; Anna Devor; Yeshaiahu Fainman. The dissertation author was the investigator and author of this material.

# CHAPTER 3

## INCREASED PENETRATION DEPTH WITH NON-DEGENERATED TWO PHOTON EXCITATION

Two-photon microscopy has been a mature technique in monitoring neuron activity and blood vessel in the past few decades but achieving the images in deeper layer is still challenging. The penetration depth for most of brain images are limited to several hundred microns with commonly used 80-MHz laser since the pump power greatly attenuated in brain tissues and thus the generated fluorescence signal could be too low for the detection. In addition to improving the collection efficiency of the system with hardware design and selecting the fluorophores with high excitation cross sections, managing to deliver more ballistic light into the deep layer can achieve better image contrast.

### 3.1 Background

As the discussion in the previous chapter, several groups have been working on maximizing excitation cross section by manipulating molecular structures in order to efficiently generate fluorescence signal and increase the penetration depth [42]. On the other hand, since the fluorescence signal generated under D-2PE is quadratically dependent on the photon flux, using pump laser with high peak power is an alternative way to yield

strong excitation. Reducing the repetition rate squeezes more energy into one pulse which ideally improves the excitation efficiency. However, taking images at low repetition rate would decrease frame rate since the system requires longer integration time. One approach to effectively increase repetition rate and maintain high pulse energy is to interleave few channels of pulses at low repetition rate [9]. Unfortunately, ensuring the stability of the pulse train and reducing the complexity of entire system are not trivial tasks. Another way to obtain laser with high peak power is to compress pulse width, but narrow pulse is usually accompanied with chromatic dispersion and wavefront distortion as laser beam propagates through the optics. Both mechanisms would affect the performance of signal generation. Although these issues could be mitigated or compensated with additional optics, it also increases the complexity of the system and induces more loss in the system. Regardless of dispersion and distortion from particular optics in the system, it is difficult to deal with inhomogeneous structures in brain tissues without preprocessing and characterizing optical properties of brain tissues. These phenomena indeed happen to hundred-femtosecond pulse lasers but shorter pulse aggravates experimental conditions. In addition, unlimitedly compressing pulse width eventually decreases excitation efficiency when the spectral bandwidth becomes wider than the excitation bandwidth. More straightforward method is to increase average power of pump laser but more heat would be induced on tissue surface and damage brain tissues [43]. Since the key is to deliver more power into deep layers, a better solution is to reduce the attenuation. The mean free path based on the scattering parameters of brain tissues increases with wavelength so that laser beams at longer wavelengths generally penetrate deeper into brain tissues. Water absorption also plays an important role in attenuation. Considering both mechanisms, there are two transparent

windows for pump wavelength in the application of brain images (Fig.3.1) [44]. Moreover, pumping fluorophores at long wavelength usually emits the reddish fluorescence which experiences less scattering in collection path even though the resolution under D-2PE is slightly worse. Recently, the imaging of mouse cortical vasculature in vivo down to  $\sim 1.6$  mm was recorded with pump wavelength at 1280 nm [7]. In this work, we propose that ND-2PE effectively increases the penetration depth in the scattering phantom. ND-2PE involves two photons with different photon energies so low energy photon (longer wavelength) can be used to compensate the loss of high energy photon (shorter wavelength).

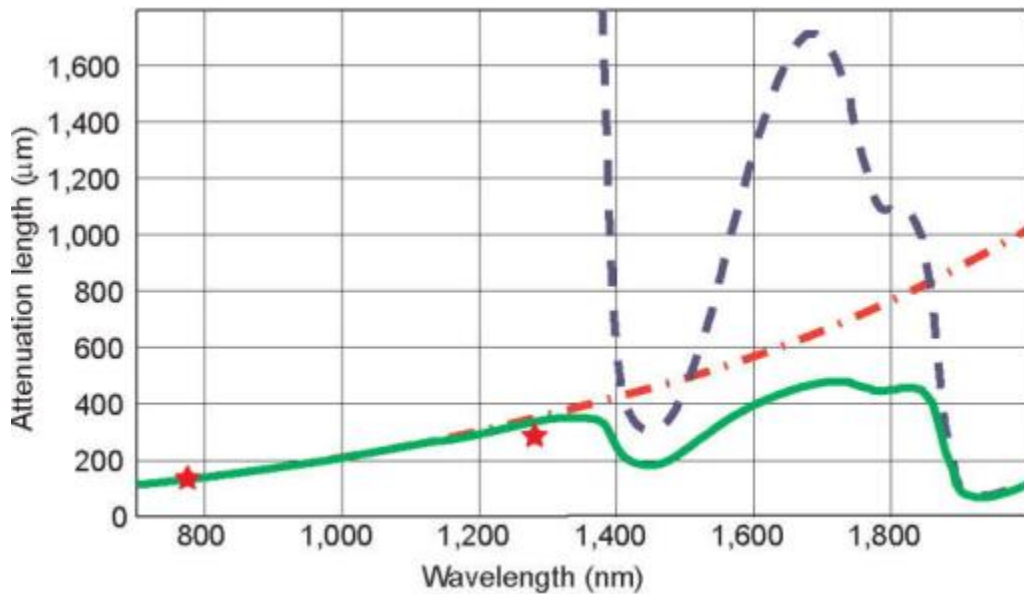


**Figure 3.1:** The attenuation length at different wavelength in brain tissues.

## **3.2 Increased penetration depth with non-degenerated two photon excitation**

### **3.2.1 Sample Preparation and Characterization Setup**

In order to demonstrate that ND-2PE increases the attenuation length by introducing additional IR beam, we designed the scattering phantom for the experiment. To emulate the scattering properties of biological tissue we used intralipid (Hospira Liposyn II 10%) diluted in distilled water with varying concentrations. The intralipid concentrations in our experiment were 0.5%, 0.75%, 1%, 1.5%, and 2% by volume. Specifically, 1% intralipid in water (by volume) has been used as a standard phantom for studies of light penetration in brain tissue [45,46]. The sample, consisting of 500  $\mu\text{M}$  fluorescein in a glass capillary, was submerged in a cuvette with intralipid solution. With the sample held in place, the intralipid cuvette was scanned along the axial direction such that the excitation lasers had to propagate through ever increasing path lengths within the scattering medium. The fluorescence intensity was measured as a function of depth within the intralipid. Instead of applying epi-illumination scheme, the fluorescence signal was collected from the side of the cuvette at 90 degrees relative to the excitation using a second objective. The whole setup is depicted in Fig. 3.2. Since the sample remained stationary, the distance between the fluorescein capillary and both microscope objectives were held constant for all data points, and the path length that the emitted light had to propagate through the scattering medium on its way to the detector also remained constant. With this collection scheme, the fluorescence attenuation remains constant for each data point. Thus, any change in fluorescence intensity resulted purely from attenuation of the excitation

SWIR and NIR beams on the way to the sample. In this experiment, the SWIR and NIR wavelength was chosen to be 825 nm and 1315 nm, respectively. To verify that both beams focused to the same focal plane, the same alignment optimization methods described in chapter 2 were applied at every depth. The excitation intensity of the NIR and SWIR beams were chosen such that the fluorescence signal of D-2PE and ND-2PE was the same entering the intralipid (i.e., zero depth). At every depth, fifty data points were collected, and from these the average fluorescence signal and its standard deviation around the mean were tabulated.

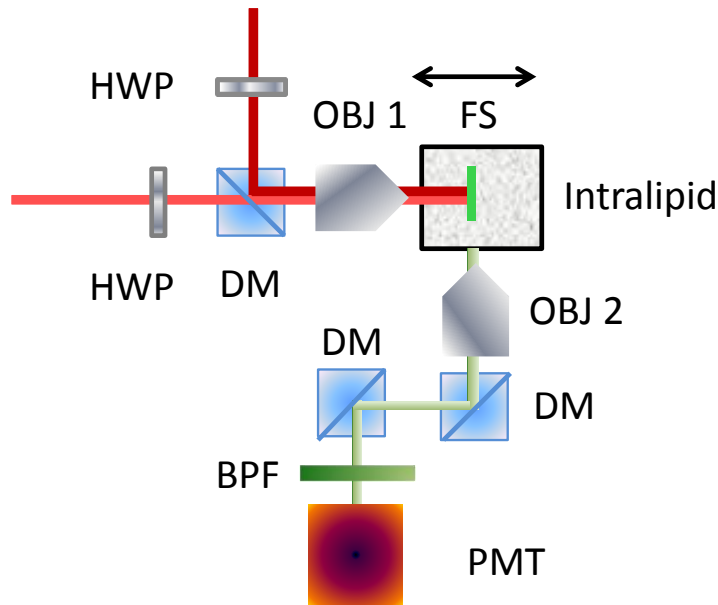


**Figure 3.2:** Experimental setup for demonstration of penetration depth of D-2PE and ND-2PE. HWP, half wave plate; DM, dichroic mirror; FS, fluorescent sample; OBJ 1, 40X microscope objective; OBJ 2, 20X microscope objective; BPF, band pass filter; PMT, photomultiplier. The arrow indicated the direction of movement of the cuvette.

For every combination of intralipid concentration, the data demonstrated a decay in the fluorescence intensity as a function of increasing depth, i.e., the distance that the excitation beams had to propagate through the scattering medium (Fig. 3.3 (a-e)). To

quantify the attenuation, we modelled this process as a Beer-Lambert Law type decay of the excitation intensity:

$$I_{NIR}(z) = I_{NIR}(0) \exp\left(\frac{-z}{\alpha_{NIR}}\right) \quad (18)$$

$$I_{SWIR}(z) = I_{SWIR}(0) \exp\left(\frac{-z}{\alpha_{SWIR}}\right) \quad (19)$$

Here  $z$  is depth,  $\alpha_{NIR}$  and  $\alpha_{SWIR}$  is the attenuation length of the NIR and SWIR beams, respectively, and  $I(0)$  is the laser intensity entering the intralipid. Substituting these equations into the appropriate expressions for the fluorescence intensity we find

$$I_{D2PE}(z) = A_D I_{NIR}^2(0) \exp\left(\frac{-2z}{\alpha_{NIR}}\right) \quad (20)$$

$$I_{ND2PE}(z) = A_{ND} I_{NIR}(0) I_{SWIR}(0) \exp\left[-z\left(\frac{1}{\alpha_{NIR}} + \frac{1}{\alpha_{SWIR}}\right)\right] \quad (21)$$

where  $A$  is a constant which contains absorption cross section, collection efficiency, fluorophore concentration and fluorescence quantum efficiency.

### 3.2.2 Demonstration of The Increased Penetration Depth with ND-2PE

To extract attenuation length of ND-2PE and D-2PE, we first normalized the fluorescence curves to express fluorescence relative to its values at zero depth (Fig. 3.3(a-e)). We then fit each curve with Eq. (20) and Eq. (21) for D-2PE (blue dots) and ND-2PE (green dots), respectively. The resulting attenuation lengths for D-2PE and ND-2PE, as well as that of each laser, are plotted as a function of intralipid concentration in Fig.3.3(f). For 1% intralipid, we find 50% improvement in the attenuation length of ND-2PE ( $235 \pm 0.8 \mu\text{m}$ ) relative to that of D-2PE ( $156 \pm 0.5 \mu\text{m}$ ). In Fig.3.3 (a-e), only the signals above the noise level were used to fit exponential function although we measured several points below the threshold.

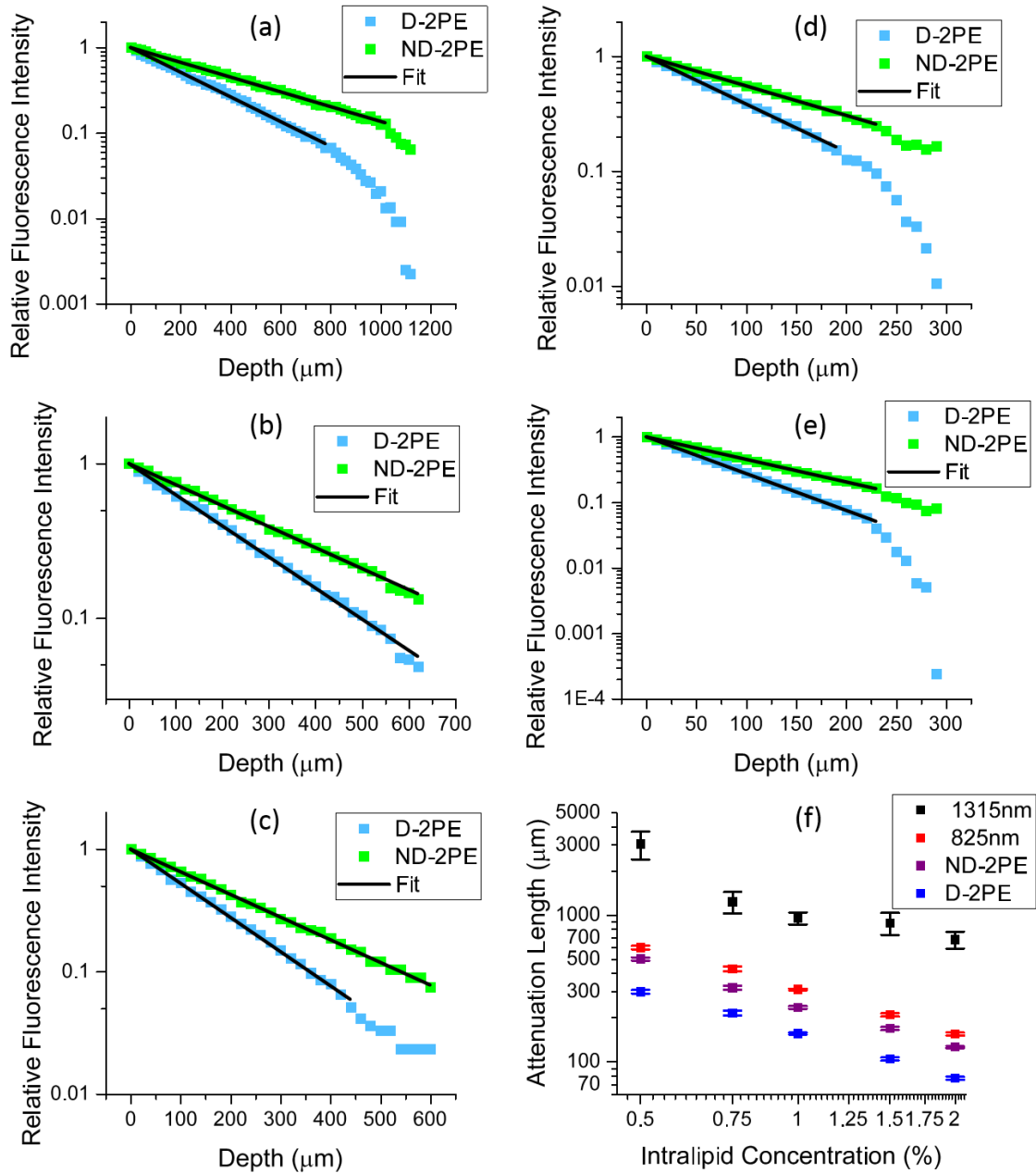


**Figure 3.3:** Relative fluorescence intensity as a function of sample depth within varying concentrations of intralipid: (a) 0.5 %, (b) 0.75%, (c) 1%, (d) 1.5 % and (e) 2%. (f) Attenuation length as a function of intralipid concentrations.

The spectroscopy measurement in chapter 2.3 shows that, with our choice of the NIR and SWIR wavelengths, the excitation cross-section for ND-2PE in the transparent

medium is lower than that for D-2PE. However, we anticipated that the efficiency of ND-2PE will be higher compared to that of D-2PE in the scattering medium, due to longer attenuation length of ND-2PE (Fig. 3.3 (f)). To investigate this hypothesis, we began with a theoretical calculation. We modeled the beam attenuation with the Beer-Lambert law using the attenuation length of D-2PE and ND-2PE from Fig. 3.3(f). In order to reveal the effect of ND-2PE, for simplicity, the photon flux of the NIR and SWIR beams were set to be equal for the D-2PE and ND-2PE before entering the scattering medium. The fluorescence signal in the simulation was normalized to the fluorescence signal of D-2PE at the entrance to the scattering medium (i.e., zero depth). The calculated result is shown in Fig. 3.4, where the blue and green curves represent the fluorescence intensity resulting from D-2PE and ND-2PE, respectively. Within about one attenuation length of the NIR beam, the lower fluorescence signal of ND-2PE is a result of its lower excitation cross-section (chapter 2.3). Past this point, the advantage of ND-2PE becomes clear. Since the fluorescence intensity depends quadratically on the intensity of the NIR beam, which experiences higher scattering, the ND-2PE signal begins to exceed that of D-2PE. This is because the SWIR beam is attenuated less during propagation in the scattering medium. At a depth of  $700 \mu\text{m}$ , where the lowest D-2PE signal could be detected experimentally in Ref. [2], the D-2PE signal drops by  $\sim 19.34 \text{ dB}$  (the red dotted line in Fig. 3.4). For the ND-2PE case, however, the same loss is calculated to occur at  $910 \mu\text{m}$  indicating  $\sim 210\text{-}\mu\text{m}$  enhancement of the penetration depth.

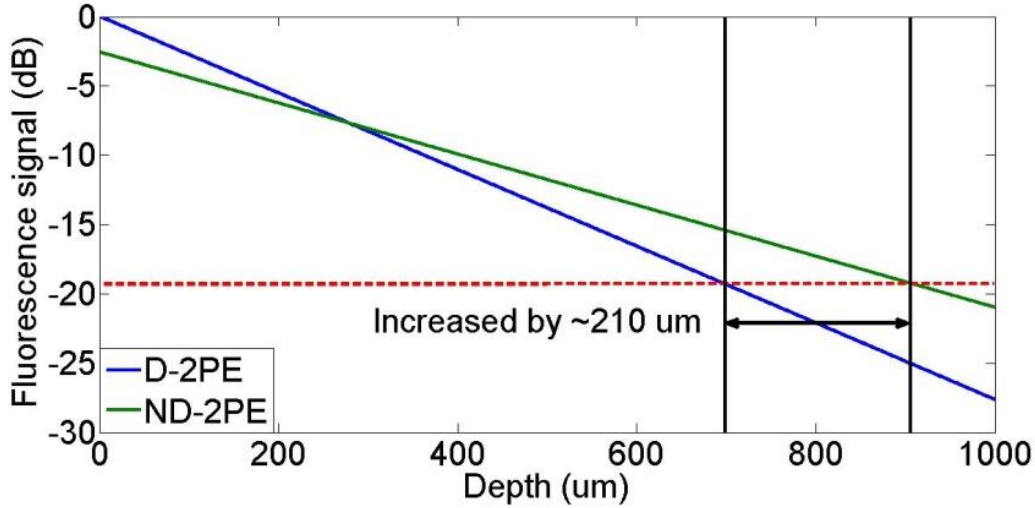


**Figure 3.4:** Simulation of the fluorescence intensity under D-2PE (blue) and ND-2PE (green) as a function of depth in the scattering medium.

### 3.2.3 Experimental Validation of Penetration Depth Increase via ND-2PE

To experimentally validate the theoretical analysis in chapter 3.2.2, we returned our setup to the original epi-illumination configuration depicted in Fig. 2.2. Measurements were performed with a fluorescein sample in 1% intralipid. The sample was submerged at varying depths in the intralipid. We started this experiment at depth zero with the NIR beam alone (D-2PE). The power of the NIR beam was increased with an increasing depth to maintain the 3dB SNR of the signal at the detector. This process was continued until the NIR power was exhausted, which set the excitation depth limit for D-2PE. For greater depths, we kept the NIR power at the maximum and introduced the SWIR beam to produce ND-2PE in addition to D-2PE. The power of the SWIR beam was increased with increasing depth to maintain the 3dB SNR of the signal at the detector. This continued until the available SWIR power was exhausted.

The results of this experiment are presented in Fig. 3.5. With our particular optical setup, we could maintain the 3dB SNR down to  $\sim 550 \mu\text{m}$  within the intralipid with D-

2PE alone. With the combination of D-2PE and ND-2PE we surpassed this barrier - increasing the maximum excitation depth to  $\sim 750 \mu\text{m}$ . Thus, under our specific conditions and target SNR, we achieved a  $\sim 200 \mu\text{m}$  increase in the excitation depth. We expect that with a more optimal choice of the excitation wavelengths and objectives, an even greater increase in penetration depth can be achieved.

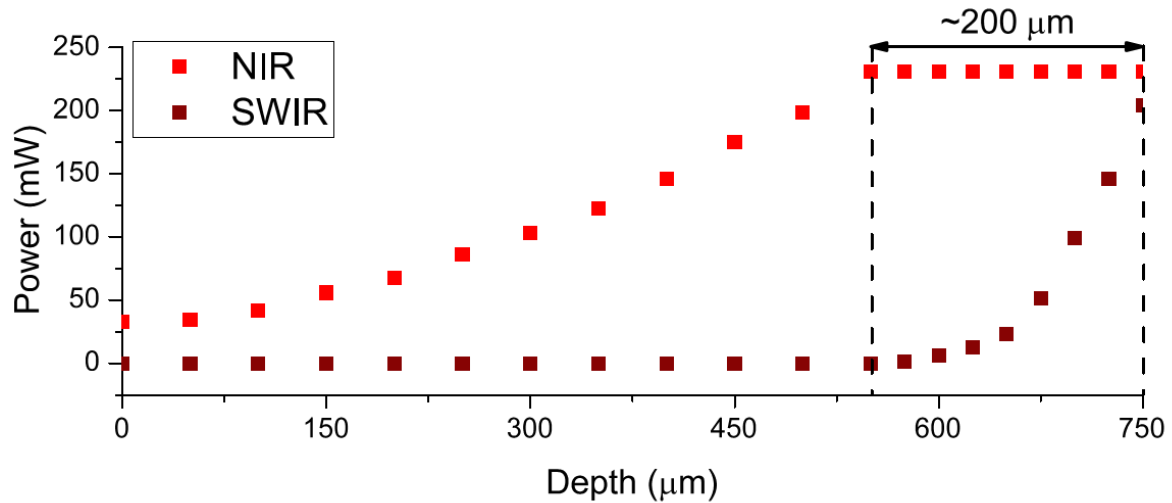


**Figure 3.5:** Experimental demonstration that ND-2PE can excite fluorescence at greater depth.

### 3.4 Discussion

In this experiment, we operated the laser at two specific wavelengths since the chosen SWIR wavelength has long attenuation length in the first transparent window and the OPO system gave maximum output power when NIR wavelength was set to 825 nm. In this experiment we chose fluorescein as the sample for investigating the increased attenuation length by introducing SWIR beam. However, the ideal samples are red fluorophores with D-2PE peak around 1013 nm which is the equivalent D-2PE wavelength of the chosen wavelength combination. In fact, not only one beam from ND-2PE can help

to increase the penetration depth. Recently, Brain Initiative Community is seeking for red fluorophores for deep image. If the excitation peaks of fluorophores will be extended to strong water absorption band (eg. excitation wavelength between 1300 nm and 1550 nm), ND-2PE can overcome this inherent problem by placing two wavelengths at the two transparent windows. Therefore, a significant improvement in attenuation length of brain images can be expected.

In chapter 3.2.2, we demonstrated that ND-2PE provided greater penetration depth in the scattering medium. Increasing the SWIR photon flux helped to compensate for the scattered loss of the NIR beam. Ultimately, this effect is limited by wavelength-specific tolerance of the tissue for laser power in the application of brain images. Further studies will be required to determine the optimal wavelength combination with proper pump power for achieving the maximum fluorescence signal without tissue damage. In our experiments, we did not optimize the spatial overlap as considering the wavefront distortion and spatial walk-off for two laser beams. Regardless of these issues, ND-2PE still provided longer penetration depth since SWIR beam delivered more power into the scattering phantom and suffered from less wavefront distortion. This feature was an evidence that SWIR beam can be used as a “guiding star” for wavefront correction of NIR beam as we discuss in chapter 2.

### 3.5 Supplementary Materials

In addition to the simulation for attenuation length at different wavelength shown in chapter 3.1, Robert Alfano' group [31] verified the attenuation properties of brain slices with different thickness. Two transparent windows became more obvious when the thickness of the brain tissue slice was increased (Fig. 3.6).

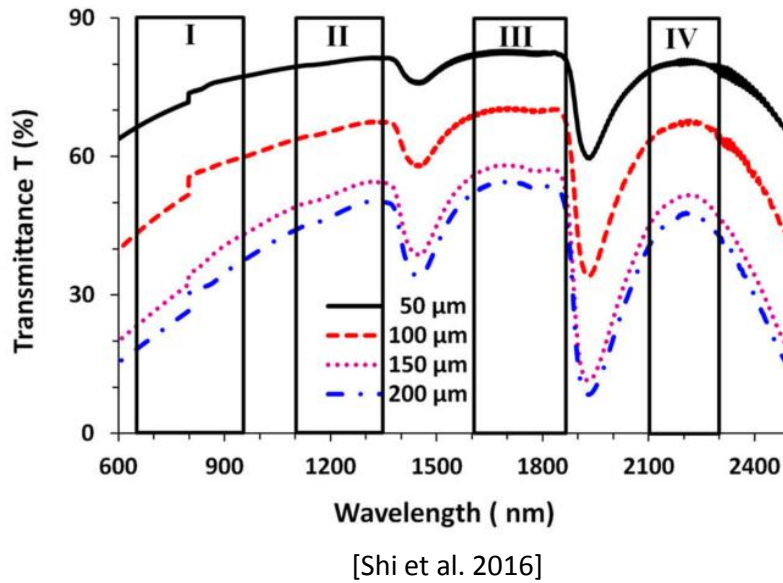


Figure 3.6: The transmission of brain tissue with different thickness.

### Acknowledgments

Chapter 3 covers the materials from "Non-degenerate 2-photon excitation in scattering medium for fluorescence microscopy" by Mu-Han Yang, Maxim Abashin, Payam Saisan, Peifan Tian, Chris Ferri, Anna Devor, and Yeshaiahu Fainman, which was published in Optics Express. The dissertation author was the primary investigator and author of this paper.

# CHAPTER 4

## REDUCTION OF OUT-OF-FOCUS EXCITATION

Plenty of works having been focusing on achieving deep brain image by increasing peak power, reducing power loss, or enhancing excitation cross section as the discussion in the previous chapters. However, recording neuron activity in deeper layer is eventually limited by out-of-focus excitation because of the degradation of signal to background ratio (SBR) when more power is applied to overcome the attenuation [47]. Especially, high scattering property in white matter results in less excitation photons reaching hippocampus and inducing strong backscattered fluorescence. This effect dominates the penetration depth in brain images. In our work, we avoided the background signal by separating two beams until they reached the focal plane.

### 4.1 Background

Out-of-focus excitation is the fundamental limit in image depth for degenerated multi-photon microscopy because SBR can not be improved by simply increasing the pump power. The reason is that the increased pump power is also accompanied with the enhancement of out-of-focus excitation. For some early studies which were operated with commonly used 80-MHz laser, the constrain of image depth was the maximum output power. However, Patrick Theer and Winfried Denk [9] numerically and experimentally

demonstrated that even without power limit, the penetration depth of degenerated two-photon microscopy is determined by the out-of-focus excitation. Fig. 4.1 shows their simulation for fluorescence generated under D-2PE at different depths. They used 0.9 as the isotropic parameter to evaluate the fluorescence generated in brain tissues. Fig 4.1 shows that the background signal can be generated from ballistic photons and scattered photons individually and the interaction between these two types of scattered photons. In their simulation, the temporal overlap for the scattered photons was also taken into account. Fig. 4.1 reveals the fact that most of the background noise is generated near the sample surface where the collection efficiency is better than that of signal emitted from the sample plane. Fig. 4.2 experimentally demonstrates that out-of-focus excitation limits the penetration depth in the beads sample which mimic real brain tissues. Although the pulse energy in their experiment was as high as  $3 \mu\text{J}$ , they could not achieve a good image contrast at the depth beyond 1.4 mm.

Consequently, more and more techniques have been developed to solve this issue. Exploring red fluorophores not only reduces the power loss but also mitigates the out-of-focus excitation since the applicable pump wavelengths locate in optical transparent windows of brain tissue ( $\sim 1300\text{-}1400 \text{ nm}$  or  $\sim 1600\text{-}1900 \text{ nm}$ ) and less scattered photons produce the out-of-focus fluorescence [2,31]. Three-photon microscopy is an alternative technique to obtain a descent SBR because of the properties of the tight excitation volume and therefore less background signal. A recent study has demonstrated the images of hippocampal neurons expressing red fluorescent protein down to 1.3 mm with pump wavelength at 1700 nm [2].

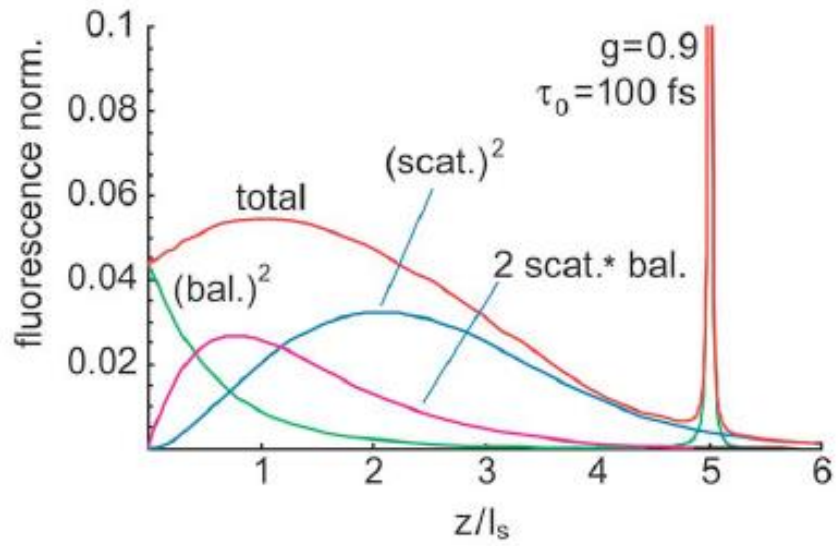


**Figure 4.1:** The simulation for fluorescence generation at different depth under D-2PE.

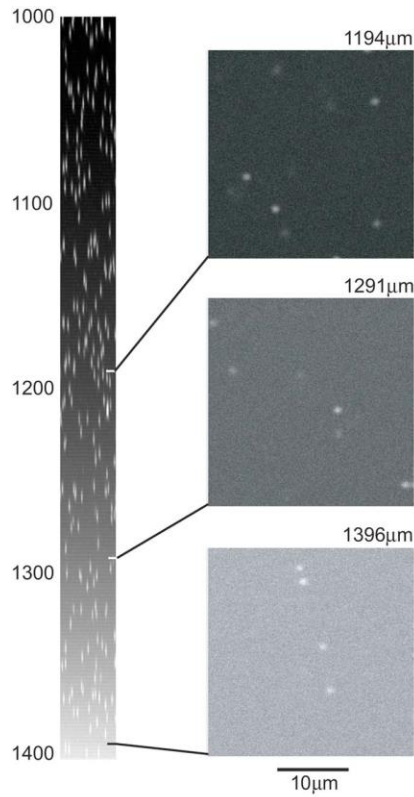


**Figure 4.2:** Fluorescence signal in beads sample under D-2PE

In addition to fluorescent probe engineering and pumping fluorophores at longer wavelength [46], temporal and phase modulation of pump laser provides another strategy to suppress unwanted fluorescence signal. Lakowicz et al. [16] and Fu et al. [18] suppressed the background noise with repetition rate detuning scheme. Kobat et al. [48] spectrally dispersed wavelength components of the pump laser until all the wavelength components arrived the sample plane. They intentionally stretched the pulse width as the laser beams propagated toward the focal plane and this method led to poor performance of the out-of-focus excitation. In contrast, the pump beam at focal plane retained a short pulse which efficiently generated fluorescence signal and yield good SBR [49]. The concern in real application is that the dispersion property would change when pump laser penetrates into different layers in mice brains. Chong et al. [50] applied spatiotemporal phase modulator in a laser scanning microscope to extract fluorescence signal generated by ballistic light from the entire signal. The operational principle was to switch between two different phase pupil filters at a fixed frequency and the proper design of the detection circuit allowed the separation of the modulated signal and non-modulated signal. In this scheme, the fluorescence signal at the focal plane was periodically generated while the out-of-focus excitation signal had different signatures in frequency domain. However, the frame rate and dwell time might be affected by the modulation frequency. Leray et al. [51] applied differential aberration to two-photon microscopy to remove the out-of-focus excitation. The concept was that a laser beam with strong aberration quenched the signal at focus more than the laser beam without aberration while the background signal was relatively

unchanged in both cases. They used a deformable mirror to control the aberration of laser beams and improved image contrast by subtracting one image from the other.

On the other hand, spatial modulation can physically reduce the background fluorescence without post-processing the image or designing detection circuit which involves complex design of optical system. Spatial modulation is not limited to degenerated multi-photon microscopy. Non-degenerated two photon microscopy also benefits from this technique due to more degrees of freedom in spatial modulation. Cambaliza, Saloma, Blanca and Saloma, Wang et al. [19,21,24] predicted and demonstrated that these constructed light techniques suppress background fluorescence generation. Most of these works focus on simulating the SBR in scattering phantom with Monte Carlo model and numerically demonstrating that spatially modulating one of the laser beams helped to reduce out-of-focus excitation [24,52]. The main idea is to avoid the beam overlap outside the sample plane since the fluorescence signal under ND-2PE is generated only when two beams are aligned spatially and temporally. Kobat et al. [48] experimentally validated that displacing two beams could reduce the excitation volume by scanning a 1- $\mu\text{m}$  fluorescent sheet in free space. Lim and Saloma had predicted that error caused by spherical aberration was reduced with ND-2PE versus D-2PE [26].

In this work, we created a turbid media consisted of fluorescence beads which has a similar scattering property to brain tissues and investigated the elimination of out-of-focus excitation under ND-2PE with side-by-side beams. Afterwards, we also investigated the out-of-focus excitation with this scheme in mice brains. The recipe of scattering phantom (beads sample) and experiment setup are described in chapter 4.2.1. We designed

a preliminary experiment in chapter 4.2.2 to show that ND-2PE with side-by-side beams created less out-of-focus fluorescence by plotting the SBR in scattering media at different depths. In chapter 4.2.3, we investigated image quality with side-by-side beams scheme by measuring the axial and lateral resolution with a 40-nm fluorescent bead. In chapter 4.2.4, we measured the ratio of D-2PE and ND-2PE cross section with a specific wavelength combination and the result indicated that ND-2PE microscopy additionally benefits from its high excitation cross section. The experimental results for images are described in chapter 4.3. We first designed a control experiment to reveal the fact that out-of-focus excitation limits images depth in scattering phantom by taking the images under D-2PE and ND-2PE with two collinear beams. To compare the images under D-2PE and ND-2PE with side-by-side beams, the images under D-2PE were conducted with pump wavelength at 909 nm which is the equivalent D-2PE wavelength of the chosen wavelength combination. We compared the SBR of the images under D-2PE and ND-2PE with side-by-side beams at the depth of 650  $\mu\text{m}$ , where increasing pump power was not able to improve the image contrast. After the demonstration with bead sample, we took images in a mouse brain under ND-2PE with side-by-side beams. However, the experiment was limited by maximum power of the IR beam. Before we reached the layer which created strong background signal, the IR power was already exhausted.

## **4.2 Materials and Methods**

### **4.2.1 Sample Preparation and Characterization Setup**

Two types of scattering phantom with 1- $\mu\text{m}$  beads were used in this work. We used the high concentrated sample for the image purpose and the low concentrated sample for

the spatial alignment. The former scattering phantom was consisted of low-melting-point agarose (0.5%; Sigma) gel containing 1  $\mu\text{m}$  diameter yellow-green (441/486) fluorescent polystyrene scattering beads (Polyscience Incorporated) at a concentration of  $5.3 \times 10^9$  beads/ml. (Polyscience Incorporated, 2.5% (W/V)) The latter scattering phantom was made of 2% Agarose gel (gel point 36 °C, Sigma) containing 1% (V/V) of 1- $\mu\text{m}$  diameter yellow-green (441/486) fluorescent polystyrene scattering beads. In our experiment, we also prepared a sample with 40-nm beads (ThermoFisher SCIENTIFIC, C14837) for characterizing the lateral and axial resolution. The concentration was  $2.1 \times 10^6$  beads/ml. In order to preserve the properties of the sample, we made 1-10 PDMS solution and put it in petri dish and let it solidify. Then we cut an 1 cm\*1 cm\*2 mm hole in middle and pour the gel and bead solution into the hole with a coverslip on top and sealed it with nail polish (Fig.4.3).

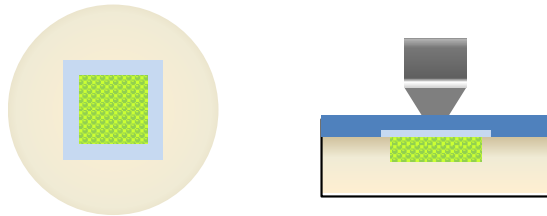


**Figure 4.3:** Bead sample. (a) top view of the sample (b) side view of the sample.

To ensure spatial overlap of the two beams at focal plane, we used the method described in chapter 2. In addition to maximize fluorescence with a fluorescein sheet for fine alignment, a more sophisticated procedure was conducted. We first focus NIR beam onto one 1- $\mu\text{m}$  bead in the low concentrated sample and optimized fluorescence signal. Then, we maximized the fluorescence signal under ND-2PE by defocusing the lenses and

tilting the mirrors in the optical path of the IR beam. The protocol required the iterative spatial and temporal alignment.

#### **4.2.2 Examination of Out-of-focus Excitation**

Before we demonstrated that ND-2PE with side-by-side beams can reduce the out-of-focus excitation in brain images, we designed a preliminary experiment to compare the out-of-focus signal under D-2PE and ND-2PE with side-by-side beams. The experimental setup is shown in Fig. 4.4. We mixed 500- $\mu$ M fluorescein with 1% intralipid in the cuvette and collected the fluorescence signal at different depths by moving the cuvette along the axis parallel to the objective lens. The collection path was divided into two paths. One the path was similar to a confocal system which included a 25- $\mu$ m pinhole before the PMT and the other path collected all the signal without pinhole. The first path with pinhole mainly detected the signal from the focal plane. We generated the fluorescence under D-2PE and ND-2PE with side-by-side beams and focus the beams with a 20X objective lens at different depths. We varied the power to maintain the same fluorescent signal collected by the first path at different depths. The Fig.4.5 shows that at the depth where the background to signal ratio equals to one under D-2PE (blue curve), ND-2PE (green curve) reduced the background signal by 40%.

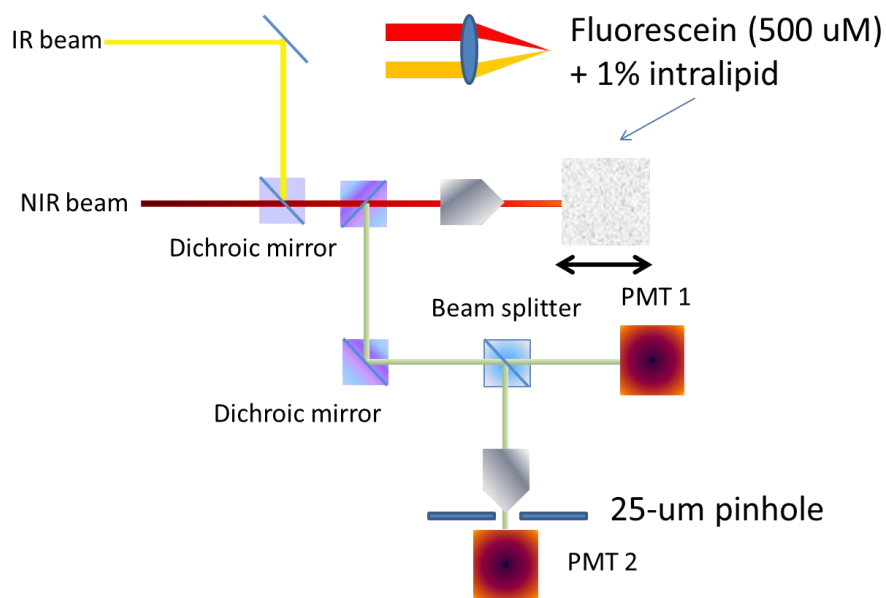


**Figure 4.4:** Experimental setup for investigating the fluorescence under D-2PE and ND-2PE with side-by-side beams

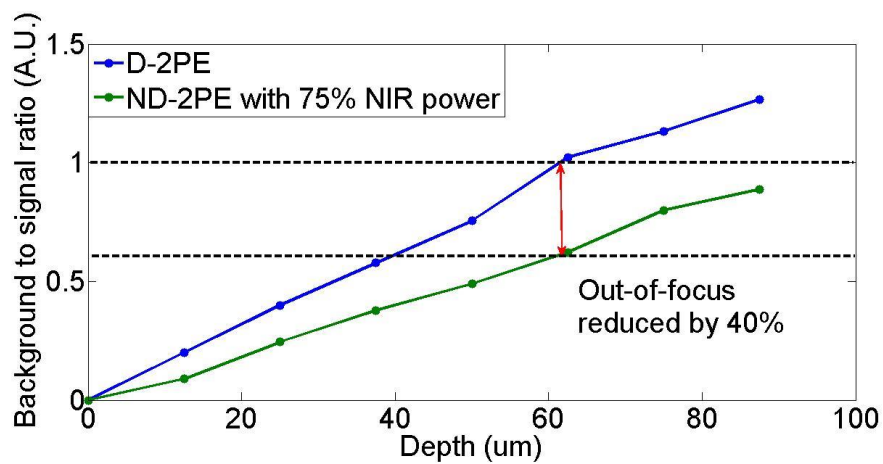


**Figure 4.5:** Experimental results of background to signal ration under D-2PE and ND-2PE with side-by-side beams

### 4.2.3 Characterization of ND-2PE volume with side-by-side beams

Similar to our previous work, we calculated the beam radius at the focal spot (i.e., beam waist) with a beam profiler (Thorlabs, BP209-IR). The calculated beam radius at the

focal spot (i.e., beam waist) was  $2.01\ \mu\text{m}$  for the NIR beam at  $780\ \text{nm}$  and the beam radius for the SWIR beam at  $1090\ \text{nm}$  was  $2.17\ \mu\text{m}$ . The intensity distribution of two beams before the objective lens is shown in Fig. 4.6. These two beams were adjusted to be well overlapped at focal plane in free space but the beam overlap degraded as these beams penetrated into the scattering media (eg. Water or tissues) due to deflection and chromatic aberration. Here, we spatially align the side-by-side beams by optimizing the signal from an  $1\text{-}\mu\text{m}$  fluorescent bead. To measure the lateral and axial resolution, we scan a  $40\ \text{nm}$  microsphere (ThermoFisher SCIENTIFIC, C14837) in transverse plane and axial plane and resolved the signal profile. Fig. 4.7 (a,b) implies that ND-2PE with the side-by-side beams still provided good excitation volume for images although both of the beams underfilled the back aperture of the objective lens. After normalizing the intensities, the measured lateral resolution was around  $1\ \mu\text{m}$  and the axial resolution was around  $5.7\ \mu\text{m}$ . The step size of the translation stage in this experiment was set to be  $40\ \text{nm}$ .

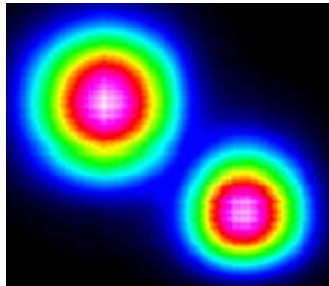
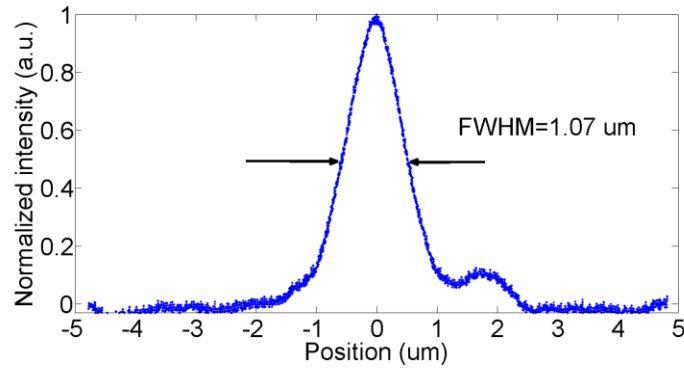
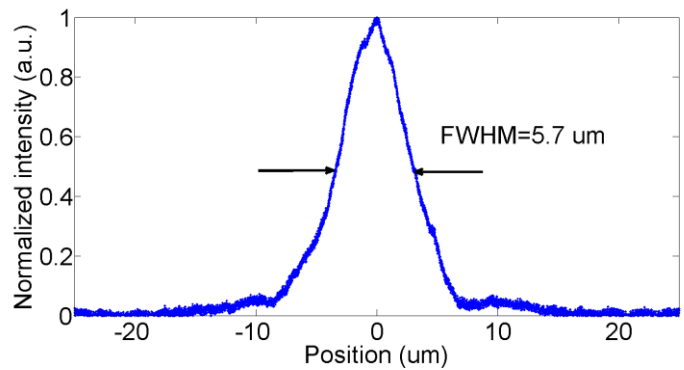


**Figure 4.6:** The intensity distribution of NIR beam and IR beam before the objective lens. The beam with larger size is the IR beam and the beam with smaller size is the NIR beam.



(a)



(b)

**Figure 4.7:** (a) lateral resolution and (b) axial resolution of ND-2PE with side-by-side beams (20X objective lens).

#### 4.2.4 ND-2PE Cross Section with Side-by-side Beams

To take the D-2PE images, we set the pump wavelength at 909 nm which was used to image the fluorescent beads in [9]. For the ND-2PE images, we selected the wavelength combination of 780 nm and 1090 nm which has the equivalent D-2PE wavelength of 909 nm. The D-2PE images with pump wavelength at 780 nm is also shown later for the comparison purpose. In our work, we investigated the ND-2PE cross section of bead sample with high concentration before we analyzed the suppression of out-of-focus excitation. Here, the measurement for the ND-2PE cross section is described as the following. We first measured the averaged fluorescence signal under D-2PE with pump

wavelength at 780 nm and ND-2PE with two collinear beams. The ratio of ND-2PE and D-2PE cross sections at 780 nm was calculated to be 1.63 based on the analysis in chapter 2. The average power of the laser with excitation wavelength at 780 nm and 1090 nm was 0.39 mW and 3.3 mW, respectively. Then, the same experimental parameters (beam size and pump power) were also applied to ND-2PE with side-by-side beams and the ratio of ND-2PE and D-2PE cross sections (excitation wavelength at 780 nm) was 1.5. The temporal profiles of fluorescence signal (time delay between two pulses) under ND-2PE with collinear beams and side-by-side beams are plot in Fig. 4.8 (a,b). The ratio of ND-2PE cross section with collinear beams and D-2PE cross section was higher due to better spatial overlap. The ratio of ND-2PE and D-2PE cross section with excitation wavelength at 909 nm was also calculated to be 1.3 which indicated ND-2PE could generate fluorescence signal more efficiently and this feature also helped to increase the penetration depth.

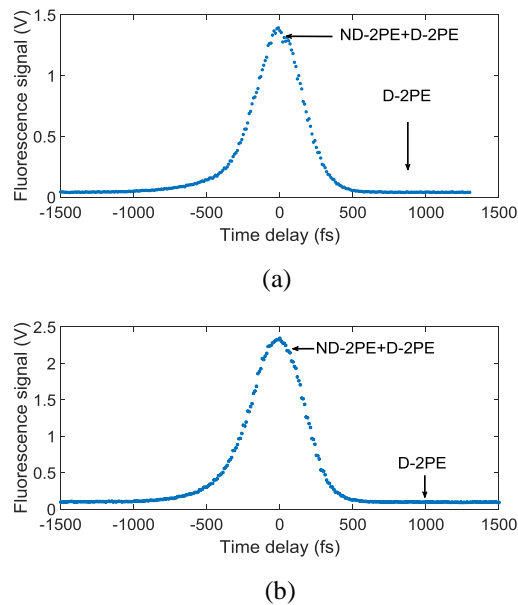


**Figure 4.8:** Fluorescence signal under ND-2PE at different time delay with (a) collinear beams and (b) side-by-side beams

### 4.3 Results

ND-2PE microscopy could benefit from the greater mean free path of SWIR beam and higher excitation cross section, but these advantages do not solve the main issues of deep image in scattering phantom. To clarify that the fundamental limit of deep image in turbid media is out-of-focus excitation, we designed a control experiment. In this experiment, a 20X water immersive objective lens (Olympus, UMPlanFLN20X) was applied to focus laser beams and collect the fluorescence signal. We took the images of a bead sample under D-2PE with the excitation wavelength at 780 nm and 909 nm separately and under ND-2PE with a specific wavelength combination (780 nm and 1090 nm) at different depths. The two laser beams for ND-2PE were collinear before the objective lens. In the ND-2PE experiment, the power of NIR beam was sufficiently low so that the signal generated under D-2PE from NIR beam was lower than the noise level. The two-dimensional images were reconstructed by plotting the fluorescent signal at every position and the results are shown in Fig. 4.9. The images size was 100  $\mu\text{m}$  by 30  $\mu\text{m}$ . For the fair comparison, we used the same excitation power in all the cases (D-2PE and ND-2PE) at the same depth. It is clear that no beads image can be observed under D-2PE with the excitation wavelength at 780 nm at the depth beyond 450  $\mu\text{m}$ . Beyond the depth of 550  $\mu\text{m}$ , beads image under D-2PE with excitation wavelength at 909  $\mu\text{m}$  could be barely observed. On the other hand, we could not get any bead images beyond the depth of 450  $\mu\text{m}$  under ND-2PE even though the excitation cross section was higher. To conclude the results, ND-2PE could efficiently generate fluorescence signal but the higher excitation cross section induced more background signal which did not improve the SBR.

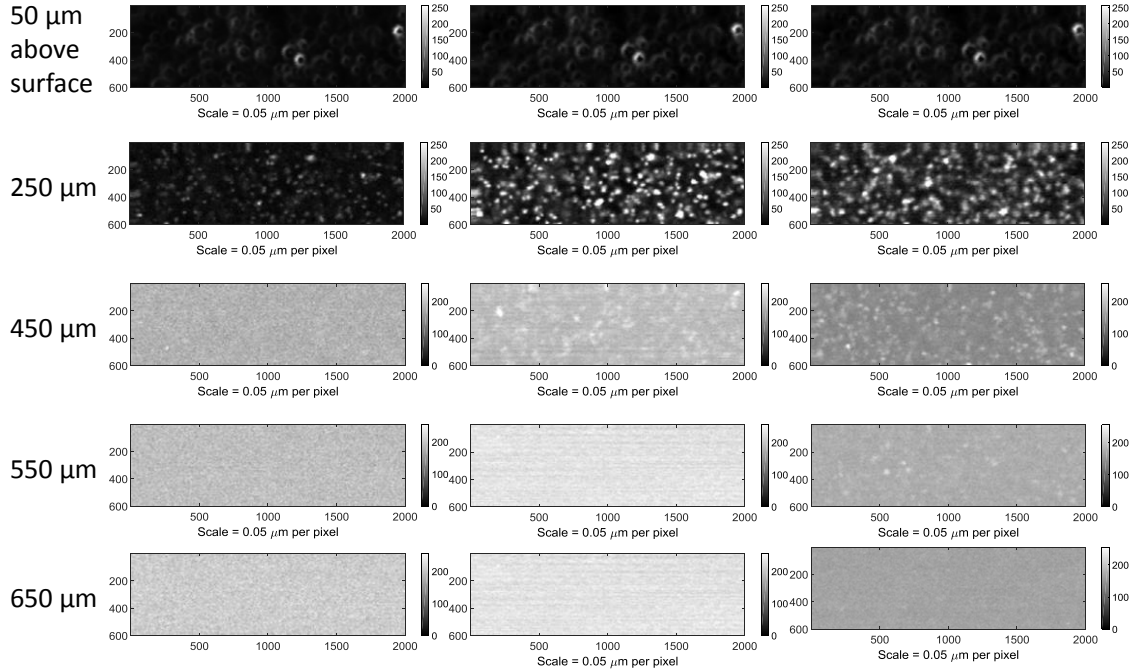


**Figure 4.9:** Images under D-2PE and ND-2PE with collinear beams at different depth (a) D-2PE (780 nm) (b) ND-2PE (780 nm and 1090 nm) (c) D-2PE (909 nm).

The next experiments were conducted in the same way, except for that ND-2PE consisted of two side-by-side beams. In Fig. 4.10, the images at the depth less than 250 μm are clear under D-2PE with excitation wavelength at 909 nm and under ND-2PE. However, when these laser beams penetrated to the depth of 450 μm, the backscattering and out-of-focus excitation dominated the image contrast. Here we noticed that the background signal of D-2PE was stronger than that of ND-2PE. As the pump beams went deeper into the sample, the images of beads at a depth of 650 μm merged with the background under D-2PE but few beads could be still observed under ND-2PE. The excitation power of ND-2PE was slightly lower than that of D-2PE since the SWIR was exhausted at this depth. In addition, the beam overlap became worse due to the scattering and this resulted in less efficient excitation and poor beam confinement. The acquired images under ND-2PE with

collinear and side-by-side beams were different in terms of image depth. The penetration depth of the collinear beams was around 450  $\mu\text{m}$  while the images at the greater depth could be achieved with side-by-side beams.

In fact, the comparison of 2D images under ND-2PE and D-2PE was not very clear at the depth of 650  $\mu\text{m}$ . Therefore, we normalized the signal by its individual peak intensity across one fluorescent bead, it revealed that SBR under D-2PE was worse than that under ND-2PE with side-by-side beams (Fig. 4.11). These experiments demonstrated that ND-2PE with side-by-side beams induced less out-of-focus excitation than D-2PE with excitation wavelength at 909 nm. At the depth of 650  $\mu\text{m}$ , we also tried to get some beads images under D-2PE by increasing the pump power but the SBR did not improve. It is possible to penetrate deeper into the scattering phantom with ND-2PE but our limitation was the maximum SWIR power in our system.

In this experiment, we observed that the beam confinement and spatial overlap degraded when the laser beams penetrated deeper in the scattering media. Applying adaptive optics is a potential solution for exploring the capability of background reduction under ND-2PE with side-by-side beams.

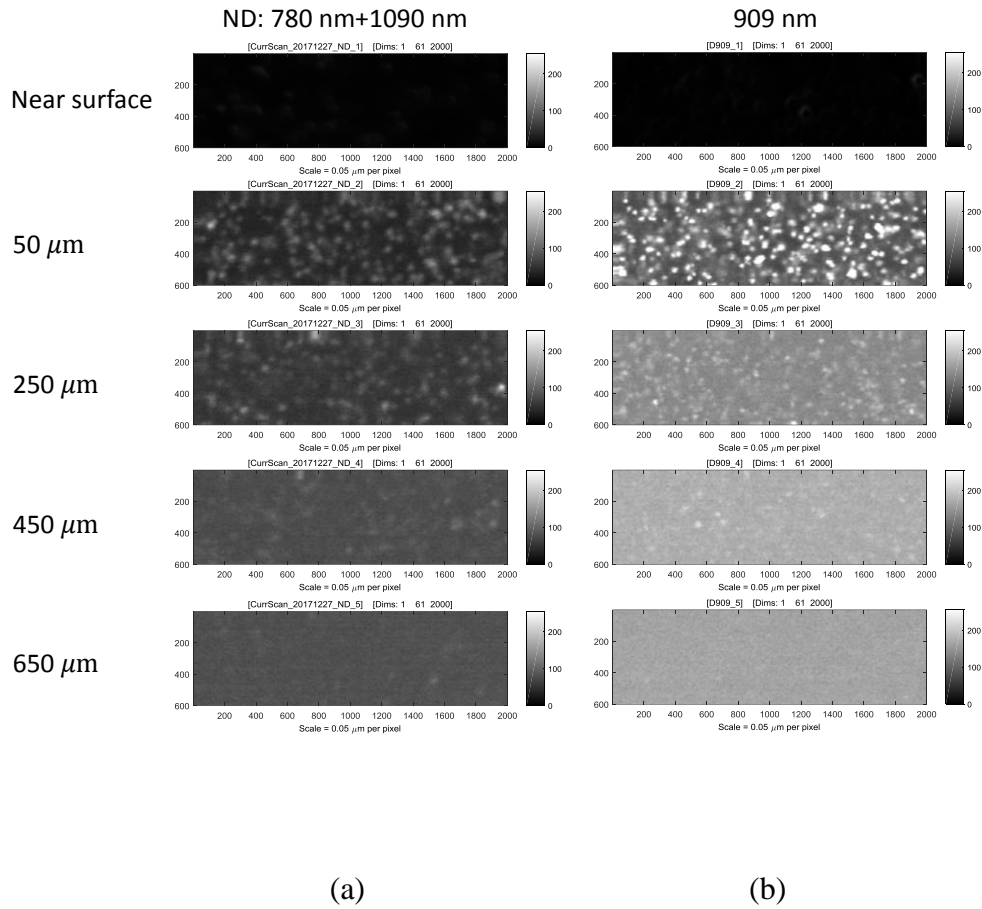


**Figure 4.10:** Images under D-2PE and ND-2PE with side-by-side beams at different depth (a) ND-2PE (780 nm and 1090 nm) (b) D-2PE (909 nm).

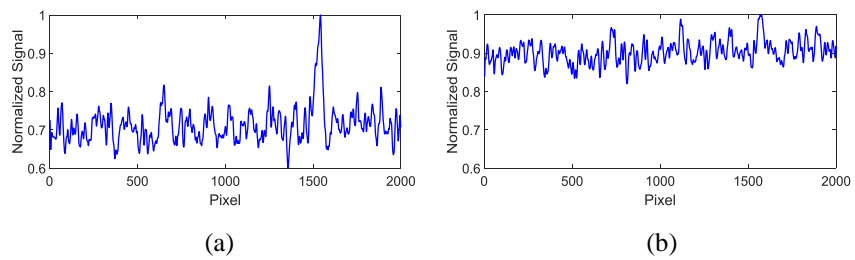


**Figure 4.11:** Line scan across one fluorescent bead under D-2PE and ND-2PE with side-by-side beams at the depth of 650  $\mu\text{m}$  (a) ND-2PE (780 nm and 1090 nm) (b) D-2PE (909 nm).

After the demonstration with beads sample, we applied this side-by-side scheme in brain images. In this experiment, the NIR wavelength was 740 nm and IR wavelength was 1230 nm. The wavelength combination minimized the out-of-focus signal generated under D-2PE from each beam based on the excitation spectrum shown in Fig. 2.6. In addition, this wavelength combination could provide the highest enhancement of ND-2PE cross section according to the theory of ISRE and the tuning range of our laser system. We took the images in an eGFP tagged mouse brain from the surface to the depth of 400  $\mu\text{m}$ . For each image experiment, we kept NIR power sufficiently low and ensured most of the fluorescence signal was from ND-2PE. (Fig. 4.12) Through all these depths, the background signal did not increase significantly. Unfortunately, before we observed strong background signal, we already exhausted all of our SWIR power ( $\sim 75$  mW after the objective lens) at the depth of 400  $\mu\text{m}$  and this limitation prevented us from investigating the reduction of background signal under ND-2PE with side-by-side beams.

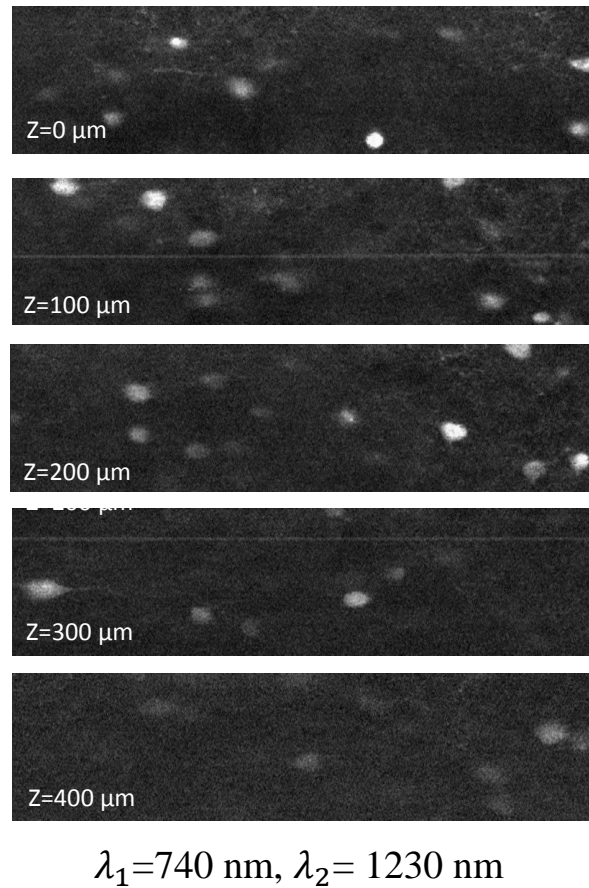


**Figure 4.10:** Images under ND-2PE with side-by-side beams

## 4.4 Discussion

Many approaches for reducing the out-of-focus excitation by spatially displacing beams have been proposed, but most of the researches focus on the analysis and the simulation results. It was mentioned in those works that experimental demonstration of ND-2PE with displaced beams is challenging because it requires to focus two beams simultaneously with two independent objective lenses at the sample plane. Using single objective lens is possible but dealing with the chromatic aberration is an issue. In addition,

these simulations were based on the assumption that the quantum efficiency of D-2PE and ND-2PE was the same but this assumption is not valid in the real application. In this work, we characterized the enhancement of ND-2PE cross section and then experimentally demonstrated that images under ND-2PE with two displaced beams could reduce the unwanted background. The difficulty in beam overlap was achieved with the assistance of an 1- $\mu\text{m}$  bead. We also investigated excitation volume with our measurement and the result indicated this technique sacrificed the resolution because both beams needed to underfill the back aperture of the objective lens. In fact, underfilling the back aperture of objective lens effectively reduced the pump intensity at focus and degraded the excitation efficiency. Using two separate objective lenses can improve the image resolution but it is not applicable to take brain image with two objective lenses with high NA.

For the experiment of brain images, the effect of reduction of out-of-focus excitation was limited by the insufficient pump power. We planned to replace the current laser system with the laser giving higher pulse energy. In addition, the detection can be modified by circuit design to increase the sensitivity. An alternative solution is to take image with red fluorophore which allows to deliver more power into brain tissues.

To further improve the performance of our system for recording neuron activities in mice brains, applying Galvo mirrors system is inevitable. However, because of the chromatic aberration, inserting a 4-f system into Galvo mirror system still needs to be investigated. Different optical path for the beams at different wavelengths would induce temporal and spatial walk-off during scanning. Applying adaptive optics is a potential

solution for correcting the spatial and temporal walk-off but the frame rate will be slowed down due to the adjustment at different deflected angles.

Another scheme of ND-2PE to reduce out-of-focus excitation is a combination of a concentric beam and a Gaussian beam. This method might be more practical as considering the issue of beam overlap. Two achievable components to generate a concentric beam are spatial light modulators and axicons but there is a trade-off between high quality beams and power loss. The other concern is that the axial resolution is worse as compared to D-2PE because it is dominated by the concentric beam.

In summary, we have experimentally demonstrated that ND-2PE with side-by-side beams provided a way to overcome the issue of low SBR in bead sample although the effect in brain image was limited by our laser power. It is possible to yield greater penetration depth in scattering phantom by increasing SWIR power without inducing too much unwanted background. On the contrary, D-2PE can not avoid inducing strong out-of-focus excitation as the pump power is increased.

## **Acknowledgements**

Chapter 4 covers the work of reduction of out-of-focus excitation which is achieved by displacing two beams. Chapter 4, in part is currently being prepared for submission for publication of the material. Mu-Han Yang; Sanaz Sadegh; Payam Saisan; Martin Thunemann; Chris Ferri; Anna Devor; Yeshaiahu Fainman. The dissertation author was the primary investigator and author of this material.

# CHAPTER 5

## CONCLUSION AND FUTURE WORKS

This thesis demonstrates three advantages of ND-2PE to achieve deep image in brain tissues: (1) The excitation cross section can be enhanced by detuning the photon energy from half of the required excitation energy. (2) The power loss of NIR beam can be compensated by introducing SWIR beam. (3) Better image contrast for deep image can be obtained by reducing the background noise with side-by-side beams.

Recently, the Brain Initiative Community is seeking for red fluorophores since the excitation and emission wavelengths provide longer attenuation length than green fluorophores. Our system for ND-2PE spectroscopy is well established and is ready for exploring red fluorophores. Since the lowest single photon allowed state of red fluorophores is closer to the ground state than that of green fluorophores, we expected more enhancement of ND-2PE cross section with the current laser system. However, for the application of brain image, the penetration depth also is limited by the attenuation length at different wavelengths and the enhancement might not be significant in brain images if the wavelength combination is properly chosen. If red fluorophores with peak excitation wavelengths between 1350 nm and 1550 nm are developed in the future, we can place two excitation wavelengths at the peaks of transparent windows (Fig. 3.1) and this wavelength

combination can circumvent the strong water band. In addition, since these two wavelengths locate outside the excitation peak, these two beams individually can only generate few amounts of fluorescence signal under D-2PE. If the scheme of displaced beams is also applied, more background signal can be reduced.

We not only demonstrated the advantages of ND-2PE but also applied ND-2PE to in vivo brain image. A prototype ND-2PE microscope was accomplished but it was not an ideal system for recording neuron activities. The current system acquires the image by scanning the sample instead of the laser beams due to the chromatic aberration and dispersion from pupil lens and scan lens in Galvo mirror system. Therefore, the frame rate of the current setup is slow. Our next step is to investigate the temporal and spatial walk-off of side-by-side beams in Galvo mirror system. Another potential scheme of displaced beams is a combination of a concentric beam and a Gaussian beam since it might be easier to deal with the misalignment in Galvo mirrors system. On the other hand, the spatial and temporal walk-off would change and the power intensity would become lower due to the scattering and aberration in brain tissues. To preserve good beam shape and optimize beam overlap, it requires to precompensate wave front of laser beams to correct the distortion in brain tissues. Although these treatments might slow down the frame rate and increase the system complexity but it is necessary for exploring the ability of ND-2PE microscopy in deep brain image. The modification of the system will include the adaptive optics in both NIR beam and SWIR beam paths.

# APPENDIX A

## INTERMEDIATE STATE RESONANCE ENHANCEMENT BY ESSENTIAL STATE MODEL

Intermediate state resonance enhancement (ISRE) occurs when photon energy of one of excitation photons approaches the energy required to excite one electron from ground state to lowest one-photon allowed state. Effectively the electron life time in virtual state is increased and this results in enhancement of absorption cross section.

### A.1 Background

To model the resonance enhancement of ND-2PE, it involves the contributions from full states but this rigorous model would make calculation more complex and time-consuming. More importantly, it leads to less intuitively physical meaning. Hales et al. proposed to apply essential-state model for simulating ISRE of two photon absorption. In their work, instead of considering the full excited states, they used the first 300 excited states and simplified the whole energy diagram into three-level energy system. This approach provided a good approximation for estimating the enhancement and a simple explanation for understanding the mechanism. There were some discrepancies between the

simulation results and their experimental results due to underestimating the effect of high-lying states, but the measurement of single-photon absorption well explained the mismatch.

## A.2 Methods

In Hales's work, they classified fluorophores into two categories, non-centrosymmetric molecules and centrosymmetric molecules. The simplified model of essential state yields two equations for calculating the absorption cross section:

$$\delta_D = K \frac{\mu_{ge}^2 \Delta\mu_{ge}^2}{\Gamma_{ge}^2} \left( \frac{1}{\hbar\omega_1} + \frac{1}{\hbar\omega_2} \right)^2 \quad (22)$$

$$\delta_T = K \frac{\mu_{ge}^2 \Delta\mu_{ee'}^2}{\Gamma_{ge}^2} \left( \frac{1}{E_{ge} - \hbar\omega_1} + \frac{1}{E_{ge} - \hbar\omega_2} \right)^2 \quad (23)$$

Where

$$K = \frac{3L_1^2 L_2^2}{5n_1 n_2 c^2 \epsilon_0 \hbar} \frac{\hbar\omega_2 (\hbar\omega_1)^2}{(\hbar\omega_1 + \hbar\omega_2)} \quad (24)$$

$\delta_D$  and  $\delta_T$  is the calculated cross section for non-centrosymmetric molecules and centrosymmetric molecules, respectively.  $\mu_{ge}$  is the transition dipole moment between the ground state and strongly one-photon allowed state which acts as an intermediate state for 2PA into the two-photon allowed states,  $\mu_{ee'}$  is the transition moment between strongly one-photon allowed state and two-photon allowed state, and  $\Delta\mu_{ge}$  is the difference between the permanent dipole moments in ground state and strongly one-photon allowed state.  $\omega_1$  and  $\omega_2$  are the photon frequencies.  $L$  is the local field factor and  $n$  the refractive index of the medium.  $\Gamma$  is the damping term. Based on the equation we simulated the IRSE of some useful fluorophores for brain image.

**Table 2.** Simulation of the IRSE for some useful fluorophores

$\lambda_{IR}$ (nm)	$\lambda_{NIR}$ (nm)	eGFP ISRE	$\lambda_{IR}$ (nm)	$\lambda_{NIR}$ (nm)	eYFP ISRE
740	1216	1.32	740	1307	1.38
750	1190	1.29	750	1277	1.35
760	1165	1.27	760	1249	1.32
770	1143	1.24	770	1223	1.29
780	1121	1.22	780	1199	1.27
790	1101	1.20	790	1176	1.24
800	1082	1.18	800	1154	1.22
810	1065	1.16	810	1134	1.20
820	1048	1.14	820	1115	1.18
830	1032	1.12	830	1097	1.16
840	1017	1.11	840	1080	1.14
850	1003	1.09	850	1064	1.13
860	989	1.08	860	1049	1.11
870	976	1.06	870	1034	1.09
$\lambda_{IR}$ (nm)	$\lambda_{NIR}$ (nm)	mCitrine ISRE	$\lambda_{IR}$ (nm)	$\lambda_{NIR}$ (nm)	mCerulean ISRE
740	1326	1.40	740	1070	1.22
750	1295	1.36	750	1050	1.20
760	1267	1.33	760	1031	1.18
770	1240	1.31	770	1013	1.16
780	1215	1.28	780	996	1.14
790	1191	1.25	790	980	1.12
800	1169	1.23	800	966	1.10
810	1149	1.21	810	951	1.09
820	1129	1.19	820	938	1.07
830	1111	1.17	830	925	1.06
840	1093	1.15	840	913	1.04
850	1077	1.13	850	902	1.03
860	1061	1.12	860	891	1.02
870	1046	1.10	870	880	1.01

### A.3 Acknowledgement

This appendix is a study for evaluating the ISRE of some useful fluorophores for brain images with essential state model. The simulation equations are referred to Hales's work and the measurement with the assistance from Chris Ferri and Sanaz Sadegh.

## Bibliography

1. C. Stosiek, O. Garaschuk, K. Holthoff, and A. Konnerth, "In vivo two-photon calcium imaging of neuronal networks," *Proc. Natl. Acad. Sci.* **100**(12), 7319–7324 (2003).
2. N. G. Horton, K. Wang, D. Kobat, C. G. Clark, F. W. Wise, C. B. Schaffer, and C. Xu, "In vivo three-photon microscopy of subcortical structures within an intact mouse brain," *Nat. Photonics* **7**(3), 205–209 (2013).
3. K. A. Kasischke, E. M. Lambert, B. Panepento, A. Sun, H. A. Gelbard, R. W. Burgess, T. H. Foster, and M. Nedergaard, "Two-photon NADH imaging exposes boundaries of oxygen diffusion in cortical vascular supply regions," *J. Cereb. Blood Flow Metab.* **31**(1), 68–81 (2011).
4. T. Takano, G.-F. Tian, W. Peng, N. Lou, D. Lovatt, A. J. Hansen, K. A. Kasischke, and M. Nedergaard, "Cortical spreading depression causes and coincides with tissue hypoxia," *Nat. Neurosci.* **10**(6), 754–762 (2007).
5. K. Nizar, H. Uhlirova, P. Tian, P. A. Saisan, Q. Cheng, L. Reznichenko, K. L. Weldy, T. C. Steed, V. B. Sridhar, C. L. MacDonald, and others, "In vivo stimulus-induced vasodilation occurs without IP<sub>3</sub> receptor activation and may precede astrocytic calcium increase," *J. Neurosci.* **33**(19), 8411–8422 (2013).
6. D. Kobat, M. E. Durst, N. Nishimura, A. W. Wong, C. B. Schaffer, and C. Xu, "Deep tissue multiphoton microscopy using longer wavelength excitation," *Opt. Express* **17**(16), 13354–13364 (2009).
7. D. Kobat, N. G. Horton, and C. Xu, "In vivo two-photon microscopy to 1.6-mm depth in mouse cortex," *J. Biomed. Opt.* **16**(10), 106014–106014 (2011).
8. R. Kawakami, K. Sawada, A. Sato, T. Hibi, Y. Kozawa, S. Sato, H. Yokoyama, and T. Nemoto, "Visualizing hippocampal neurons with in vivo two-photon microscopy using a 1030 nm picosecond pulse laser," *Sci. Rep.* **3**, (2013).
9. P. Theer and W. Denk, "On the fundamental imaging-depth limit in two-photon microscopy," *JOSA A* **23**(12), 3139–3149 (2006).
10. C. Xu, R. M. Williams, W. Zipfel, and W. W. Webb, "Multiphoton excitation cross-sections of molecular fluorophores," *Bioimaging* **4**(3), 198–207 (1996).

11. C. Xu, W. Zipfel, J. B. Shear, R. M. Williams, and W. W. Webb, "Multiphoton fluorescence excitation: new spectral windows for biological nonlinear microscopy," *Proc. Natl. Acad. Sci.* **93**(20), 10763–10768 (1996).
12. R. P. Barretto, T. H. Ko, J. C. Jung, T. J. Wang, G. Capps, A. C. Waters, Y. Ziv, A. Attardo, L. Recht, and M. J. Schnitzer, "Time-lapse imaging of disease progression in deep brain areas using fluorescence microendoscopy," *Nat. Med.* **17**(2), 223–228 (2011).
13. A. Mizrahi, J. C. Crowley, E. Shtoyerman, and L. C. Katz, "High-resolution in vivo imaging of hippocampal dendrites and spines," *J. Neurosci.* **24**(13), 3147–3151 (2004).
14. L. V. Wang and S. Hu, "Photoacoustic tomography: in vivo imaging from organelles to organs," *Science* **335**(6075), 1458–1462 (2012).
15. J. M. Hales, D. J. Hagan, E. W. Van Stryland, K. J. Schafer, A. R. Morales, K. D. Belfield, P. Pacher, O. Kwon, E. Zojer, and J.-L. Brédas, "Resonant enhancement of two-photon absorption in substituted fluorene molecules," *J. Chem. Phys.* **121**(7), 3152–3160 (2004).
16. J. R. Lakowicz, I. Gryczynski, H. Malak, and Z. Gryczynski, "Two-Color Two-Photon Excitation of Fluorescence," *Photochem. Photobiol.* **64**(4), 632–635 (1996).
17. A. Rapaport, F. Szipöcs, and M. Bass, "Dependence of two-photon-absorption-excited fluorescence on the angle between the linear polarizations of two intersecting beams," *Appl. Phys. Lett.* **82**(26), 4642–4644 (2003).
18. D. Fu, T. Ye, T. E. Matthews, G. Yurtsever, and W. S. Warren, "Two-color, two-photon, and excited-state absorption microscopy," *J. Biomed. Opt.* **12**(5), 054004–054004 (2007).
19. M. O. Cambaliza and C. Saloma, "Advantages of two-color excitation fluorescence microscopy with two confocal excitation beams," *Opt. Commun.* **184**(1), 25–35 (2000).
20. C. Ibanez-Lopez, I. Escobar, G. Saavedra, and M. Martinez-Corral, "Optical-sectioning improvement in two-color excitation scanning microscopy," *Microsc. Res. Tech.* **64**(2), 96–102 (2004).
21. C. M. Blanca and C. Saloma, "Two-color excitation fluorescence microscopy through highly scattering media," *Appl. Opt.* **40**(16), 2722–2729 (2001).

22. F. Xiao, G. Wang, and Z. Xu, "Superresolution in two-color excitation fluorescence microscopy," *Opt. Commun.* **228**(4), 225–230 (2003).
23. M. T. Caballero, P. Andrés, A. Pons, J. Lancis, and M. Martínez-Corral, "Axial resolution in two-color excitation fluorescence microscopy by phase-only binary apodization," *Opt. Commun.* **246**(4), 313–321 (2005).
24. C. Wang, L. Qiao, Z. Mao, Y. Cheng, and Z. Xu, "Reduced deep-tissue image degradation in three-dimensional multiphoton microscopy with concentric two-color two-photon fluorescence excitation," *JOSA B* **25**(6), 976–982 (2008).
25. S. Deng, L. Liu, G. Wang, R. Li, and Z. Xu, "Three-dimensional superresolution in two-color excitation fluorescence microscopy using theta illumination method," *Opt.-Int. J. Light Electron Opt.* **121**(8), 726–731 (2010).
26. M. Lim and C. Saloma, "Primary spherical aberration in two-color (two-photon) excitation fluorescence microscopy with two confocal excitation beams," *Appl. Opt.* **42**(17), 3398–3406 (2003).
27. S. Quentmeier, S. Denicke, J.-E. Ehlers, R. A. Niesner, and K.-H. Gericke, "Two-color two-photon excitation using femtosecond laser pulses," *J. Phys. Chem. B* **112**(18), 5768–5773 (2008).
28. S. Quentmeier, S. Denicke, and K.-H. Gericke, "Two-color two-photon fluorescence laser scanning microscopy," *J. Fluoresc.* **19**(6), 1037–1043 (2009).
29. T. Robinson, P. Valluri, G. Kennedy, A. Sardini, C. Dunsby, M. A. Neil, G. S. Baldwin, P. M. French, and A. J. de Mello, "Analysis of DNA binding and nucleotide flipping kinetics using two-color two-photon fluorescence lifetime imaging microscopy," *Anal. Chem.* **86**(21), 10732–10740 (2014).
30. P. Mahou, M. Zimmerley, K. Loulier, K. S. Matho, G. Labroille, X. Morin, W. Supatto, J. Livet, D. Débarre, and E. Beaurepaire, "Multicolor two-photon tissue imaging by wavelength mixing," *Nat. Methods* **9**(8), 815–818 (2012).
31. L. Shi, L. A. Sordillo, A. Rodríguez-Contreras, and R. Alfano, "Transmission in near-infrared optical windows for deep brain imaging," *J. Biophotonics* **9**(1–2), 38–43 (2016).
32. H. K. Tsang, C. S. Wong, T. K. Liang, I. E. Day, S. W. Roberts, A. Harpin, J. Drake, and M. Asghari, "Optical dispersion, two-photon absorption and self-phase modulation in silicon waveguides at 1.5  $\mu$  m wavelength," *Appl. Phys. Lett.* **80**(3), 416–418 (2002).

33. M. Albota, D. Beljonne, J.-L. Brédas, J. E. Ehrlich, J.-Y. Fu, A. A. Heikal, S. E. Hess, T. Kogej, M. D. Levin, and S. R. Marder, "Design of organic molecules with large two-photon absorption cross sections," *Science* **281**(5383), 1653–1656 (1998).
34. "Cho: Nonlinear Optical and Two-Photon Absorption... - Google Scholar," [https://scholar.google.com/scholar\\_lookup?hl=en&publication\\_year=2002&pages=3907&issn=0947-6539&author=B.+R.++Choauthor=M.+J.++Piaoauthor=K.+H.++Sonaauthor=S.+H.++Leeauthor=S.+J.++Yoonauthor=S.-J.++Jeonauthor=M.++Cho](https://scholar.google.com/scholar_lookup?hl=en&publication_year=2002&pages=3907&issn=0947-6539&author=B.+R.++Choauthor=M.+J.++Piaoauthor=K.+H.++Sonaauthor=S.+H.++Leeauthor=S.+J.++Yoonauthor=S.-J.++Jeonauthor=M.++Cho).
35. D. R. Miller, J. W. Jarrett, A. M. Hassan, and A. K. Dunn, "Deep tissue imaging with multiphoton fluorescence microscopy," *Curr. Opin. Biomed. Eng.* **4**, 32–39 (2017).
36. D. G. Rosenegger, C. H. T. Tran, J. LeDue, N. Zhou, and G. R. Gordon, "A high performance, cost-effective, open-source microscope for scanning two-photon microscopy that is modular and readily adaptable," *PloS One* **9**(10), e110475 (2014).
37. M.-H. Yang, M. Abashin, P. A. Saisan, P. Tian, C. G. Ferri, A. Devor, and Y. Fainman, "Non-degenerate 2-photon excitation in scattering medium for fluorescence microscopy," *Opt. Express* **24**(26), 30173–30187 (2016).
38. C. Xu and W. W. Webb, "Measurement of two-photon excitation cross sections of molecular fluorophores with data from 690 to 1050 nm," *JOSA B* **13**(3), 481–491 (1996).
39. L. Shi, A. Rodríguez-Contreras, and R. R. Alfano, "Gaussian beam in two-photon fluorescence imaging of rat brain microvessel," *J. Biomed. Opt.* **19**(12), 126006–126006 (2014).
40. L.-C. Cheng, N. G. Horton, K. Wang, S.-J. Chen, and C. Xu, "Measurements of multiphoton action cross sections for multiphoton microscopy," *Biomed. Opt. Express* **5**(10), 3427–3433 (2014).
41. M. Drobizhev, S. Tillo, N. S. Makarov, T. E. Hughes, and A. Rebane, "Absolute two-photon absorption spectra and two-photon brightness of orange and red fluorescent proteins," *J. Phys. Chem. B* **113**(4), 855–859 (2009).
42. "Birge: Semiclassical time-dependent theory of two-pho... - Google Scholar," [https://scholar.google.com/scholar\\_lookup?hl=en&publication\\_year=1986&pages=639&issn=0020-7608&author=R.+R.++Birge+author=B.+M.++Pierce](https://scholar.google.com/scholar_lookup?hl=en&publication_year=1986&pages=639&issn=0020-7608&author=R.+R.++Birge+author=B.+M.++Pierce).
43. D. Davalos, J. Grutzendler, G. Yang, J. V. Kim, Y. Zuo, S. Jung, D. R. Littman, M. L. Dustin, and W.-B. Gan, "ATP mediates rapid microglial response to local brain injury in vivo," *Nat. Neurosci.* **8**(6), 752 (2005).

44. R. Wu, Q. Zhan, H. Liu, X. Wen, B. Wang, and S. He, "Optical depletion mechanism of upconverting luminescence and its potential for multi-photon STED-like microscopy," *Opt. Express* **23**(25), 32401–32412 (2015).
45. S. T. Flock, S. L. Jacques, B. C. Wilson, W. M. Star, and M. J. van Gemert, "Optical properties of Intralipid: a phantom medium for light propagation studies," *Lasers Surg. Med.* **12**(5), 510–519 (1992).
46. G. Hong, S. Diao, J. Chang, A. L. Antaris, C. Chen, B. Zhang, S. Zhao, D. N. Atochin, P. L. Huang, K. I. Andreasson, and others, "Through-skull fluorescence imaging of the brain in a new near-infrared window," *Nat. Photonics* **8**(9), 723–730 (2014).
47. P. Theer, M. T. Hasan, and W. Denk, "Two-photon imaging to a depth of 1000  $\mu\text{m}$  in living brains by use of a Ti: Al<sub>2</sub>O<sub>3</sub> regenerative amplifier," *Opt. Lett.* **28**(12), 1022–1024 (2003).
48. D. Kobat, G. Zhu, and C. Xu, "Background Reduction with Two-Color Two-Beam Multiphoton Excitation," in *Biomedical Optics* (Optical Society of America, 2008), p. BMF6.
49. G. Zhu, J. Van Howe, M. Durst, W. Zipfel, and C. Xu, "Simultaneous spatial and temporal focusing of femtosecond pulses," *Opt. Express* **13**(6), 2153–2159 (2005).
50. S. P. Chong, C. H. Wong, K. F. Wong, C. J. Sheppard, and N. Chen, "High-speed focal modulation microscopy using acousto-optical modulators," *Biomed. Opt. Express* **1**(3), 1026–1037 (2010).
51. A. Leray, K. Lillis, and J. Mertz, "Enhanced background rejection in thick tissue with differential-aberration two-photon microscopy," *Biophys. J.* **94**(4), 1449–1458 (2008).
52. C. M. Blanca and C. Saloma, "Monte Carlo analysis of two-photon fluorescence imaging through a scattering medium," *Appl. Opt.* **37**(34), 8092–8102 (1998).